EUMETSAT ECMWF

EUMETSAT/ECMWF Fellowship Programme Research Report

RR65

Improving the Ocean Temperature in a Coupled Atmosphere-Ocean System using Microwave Imager Observations

Tracy Scanlon, Philip Browne, Alan Geer, Niels Bormann

September 2025

Series: EUMETSAT/ECMWF Fellowship Programme Research Reports

A full list of ECMWF Publications can be found on our web site under:
http://www.ecmwf.int/en/publications/

Contact: library@ecmwf.int

European Centre for Medium Range Weather Forecasts, Shinfield Park, Reading, RG2 9AX, UK

Contents

Executive Summary

Knowledge of the ocean temperature is vital to the accurate use of satellite radiances in weather forecasting and it helps improve the quality of forecasts for the ocean and atmosphere. Recent work has shown that a sink variable approach can be used in atmospheric data assimilation to extract information about the ocean temperature from satellite-borne instruments measuring in the microwave range. In the present work, we build on these developments to include, for the first time, ocean temperature information from microwave imager radiances in ECMWF's ocean analysis. This is achieved via the assimilation of radiances in a coupled atmosphere/ocean assimilation system.

Demonstrating the use of such information from satellite-borne instruments measuring in the microwave range is not only important for current instruments, but will also enhance the exploitation of upcoming sensors such as the Copernicus Imaging Microwave Radiometer (CIMR) from the European Space Agency (ESA) and the Microwave Imager / Ice Cloud Imager (MWI/ICI) from the European Organisation for the Exploitation of Meteorological Satellites (EUMETSAT).

At cycle 50r1 of the ECMWF Integrated Forecast System, the coupling between the atmosphere and the ocean has been developed at the level of the outer loop of the atmospheric data assimilation. This allows information to be passed from the atmosphere to the ocean and back again within one data assimilation window. The work presented here uses this method to pass skin temperature estimates derived from microwave imagers (AMSR2 and GMI) to the ocean data assimilation system. The updated ocean state is then passed back to the atmospheric data assimilation system. At the current stage of development the ocean is re-initialised every 24 hours from a separate 8-12 day window ocean analysis, which depends on external ocean temperature retrieval products.

The current work demonstrates that the use of these skin temperature estimates improve the fit of the ocean to ARGO float observations, resulting in up to 4% improvements in the Eastern Tropical Pacific. Improvements in the modelled SKT are also recorded indirectly through improvements in the fit of significant wave height observations and infra-red channels sensitive to the surface on-board geostationary satellites.

In terms of the forecast, the most significant changes in the mean field and improvements to the forecast verification are apparent in the medium range (2 to 6 days). Statistically significant improvements in the Root Mean Squared Error (RMSE) are seen in the tropics for relative humidity at the surface and in the Southern Hemisphere for temperature, vector winds and geopotential height in the upper atmosphere.

In the long run, as the methods used in this work are further developed and more observations become available, it may be possible to cut the dependence on the 8-12 day external ocean analysis and to fully constrain the ocean within the atmospheric 12 hour assimilation window. This scenario would be expected to extract even more benefit from the skin temperature estimates and would negate the need to use external ocean temperature products.

Plain English Summary

The temperature of the oceans plays a key role in the Earth system. Accurate, up-to-date knowledge of this parameter is important to ensure high quality weather forecasts. Recent work at ECMWF has allowed the atmospheric model and ocean model to interact by passing information derived in the atmospheric model to the ocean model.

Using information from microwave instruments on-board satellites, it is demonstrated here that passing this information to the ocean allows improvements not only in the ocean system but also in the atmospheric system. This results in improvements in the overall weather forecast, particularly in the medium range (2 to 6 days).

1 Introduction

The European Centre for Medium Range Weather Forecasts (ECMWF) Integrated Forecast System (IFS) is a global Numerical Weather Prediction (NWP) system which utilises Data Assimilation (DA) to generate initial conditions for short- to medium-range weather forecasts. In NWP, and the Earth system in general, the temperature of the ocean plays a vital role in regulating air-sea fluxes. The temperature of the very top layer of the ocean, referred to as the Skin Temperature (SKT), is commonly used as a boundary condition for the atmosphere, feeding into the NWP model as well as being an input to the simulation of satellite radiances used in DA.

At the current operational cycle (cycle 49r1, ECMWF, 2024), the IFS comprises one DA system providing the atmospheric forecast which is supported by the ocean DA system which ingests data from Level 3 SST products. The atmosphere and ocean DA systems are weakly coupled (Browne *et al.*, 2019), with the ocean and atmospheric analyses providing boundary conditions for each other in a lagged manner, slowing the flow of information between the two components. As part of the upgrade to cycle 49r2, coupled trajectories (de Rosnay *et al.*, 2022) were introduced which allow interaction between the model components.

At ECMWF, recent work (Scanlon *et al.*, 2024) demonstrated that the SKT can be derived from microwave (MW) imagers by using an observation-space sink variable approach within the atmospheric DA component. This sink variable approach allows the SKT to vary within the observation operator, RTTOV (Saunders *et al.*, 2020), to provide an updated SKT estimate consistent with the observations. In the sink variable approach, the improvements to the SKT estimates are discarded at the end of each DA window and, therefore, can only affect the analysis.

However, the upgrade to cycle 50r1 allows the SKT estimates to be passed to the ocean DA system (NEMOVAR, Mogensen and Balmaseda, 2012). This process allows these observations to affect the analysed ocean state and hence improve the overall DA and forecast. The long-term aim of implementing this type of coupling is to replace the use of external background ocean temperature information within the IFS (de Rosnay *et al.*, 2022; McNally *et al.*, 2022).

In this report, the method for passing the updated SKT to the ocean DA system is described (Section 2) and the resultant updated SKT is then presented in terms of increments (Section 3). The impact of this process is then discussed in terms of the ocean state (Section 4) and the atmospheric analysis (Sections 5). Finally, the conclusions and prospects for further work are considered (Section 6).

2 Method

2.1 Coupling between the Atmosphere and Ocean

In the IFS (as of cycle CY50r1), the atmosphere and ocean DA systems are able to pass information to one another through the use of coupled trajectories (de Rosnay *et al.*, 2022). This coupling method allows information derived in the atmosphere to be used as observations in the ocean DA system. Figure 1 summarises the atmosphere-ocean coupled system.

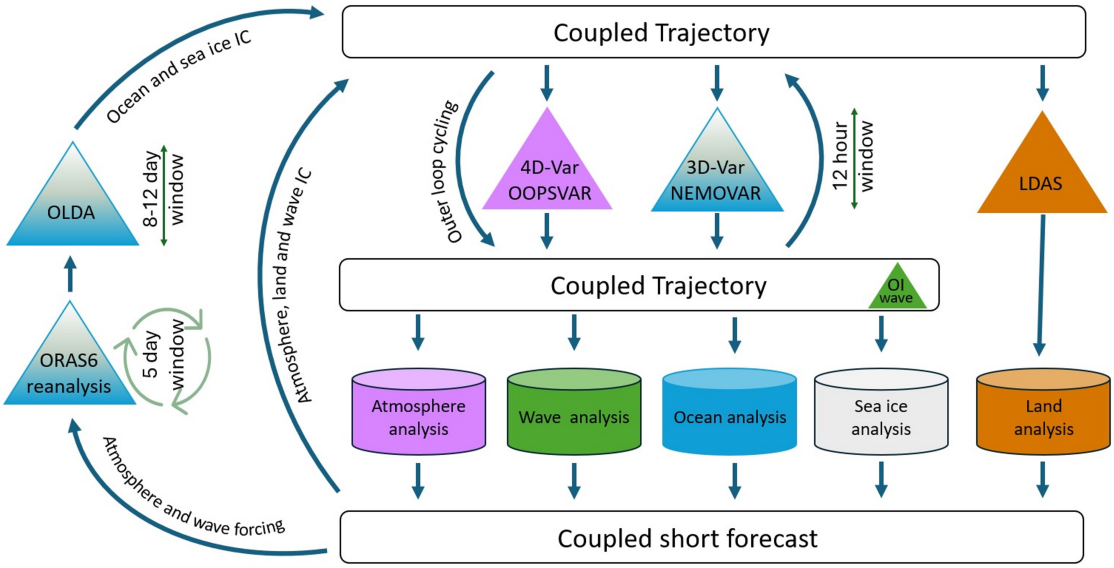

Figure 1: Outer loop coupling in the ECWMF IFS showing the relationship between the atmospheric and ocean DA systems. Updated from de Rosnay *et al.* (2022) (Courtesy of Philip Browne).

The atmospheric DA is run within 12 hour windows[1]: the 00 UTC window running from 21h to 9h and the 12 UTC window running from 9h to 21h. The ocean state at the start of the 12 UTC window is provided by the external input data stream. Within each of these DA windows, there are four outer loops (coupled model trajectories) followed by independent inner loops (minimisations) of the ocean and atmosphere DA systems.

Within the atmospheric DA system, SKT estimates are generated from the MW instruments using a sink variable approach which is referred to as the TOVS Control Variable (TOVSCV) (see Massart *et al.*, 2021; Scanlon *et al.*, 2024, for a complete description). The TOVSCV can be summarised as adding the SKT estimates (in observation space) to the control vector to allow it to be optimised along with the atmospheric model fields. As per the model fields, the SKT estimates are adjusted to provide the optimal estimate for that field of view (i.e. across all channels for a sensor).

The ocean DA system uses NEMOv4.0.6 as the underlying ocean and sea-ice model and the DA part of the system is NEMOVAR which is a 3D-Var system based on the First Guess at Appropriate Time (FGAT) method (e.g. Mogensen and Balmaseda, 2012). Once the ocean DA system has run, the updated ocean state is passed back to the atmosphere.

Every 24 hours, in order to appropriately constrain the ocean, the ocean model is reinitialised from the

[1]For the Long Window Data Assimilation (LWDA) configuration used here.

input ocean data stream. Due to this reinitialisation, while the forecast can be influenced by the updated ocean state in both the 12 UTC and 00 UTC cycles, the background can only be influenced in the 00 UTC cycle.

2.2 Estimating Skin Temperature from MW Imagers

Using the TOVSCV approach, SKT estimates are derived (see Scanlon *et al.*, 2024) from AMSR2 (Okuyama and Imaoka, 2015; Kazumori *et al.*, 2016) and GMI (Lean *et al.*, 2017). AMSR2 is a conical scanning radiometer on-board the Global Change Observation Mission for Water (GCOM-W) satellite which has a polar orbit with a 13.30 equatorial crossing time (ECT) for the ascending node (i.e. the part of the orbit where the satellite is travelling northwards). GMI (Draper and Newell, 2018) is a conical scanning radiometer on-board the GPM satellite which has an orbit inclined at 65° (i.e. observing the tropics and mid-latitudes but has no coverage beyond around 70° and has no fixed ECT). Further information on the implementation of these instruments in the IFS can be found in Kazumori *et al.* (2014), Kazumori *et al.* (2016), Lean *et al.* (2017) and Scanlon *et al.* (2024).

AMSR2 and GMI were chosen due to the availability of the low frequency channels 6.9v (AMSR2) and 10.65v GHz (AMSR2 and GMI), which are known to have sensitivity to ocean temperature (see Scanlon *et al.*, 2024; Kilic *et al.*, 2021; Shibata, 2013). Scanlon *et al.* (2024) demonstrates that the use of the 6.9v and 10.65v GHz channels allow the generation of realistic SKT information within the atmospheric DA system.

Observations from AMSR2 and GMI are processed at ECMWF under all-sky (clear and cloudy) conditions (Geer *et al.*, 2022; Bauer *et al.*, 2010; Geer *et al.*, 2010; Geer and Bauer, 2010, 2011). The observations are subject to preliminary screening and then "superobbed", i.e. averaged, onto a 40 km Gaussian grid. The superobs are then "thinned" with 7 in every 8 points marked as 'not for use' in the atmospheric DA, leading to a spacing of the assimilated radiances of 110 km. Further details on superobbing and thinning for MW imagers are available in Geer (2024).

After the superobbing and thinning processes, a range of further screening criteria are applied. The background check (BgQC) excludes data if the magnitude of the departure normalised by the observation error exceeds a factor, where the factor is specified for each sensor and channel. For AMSR2 and GMI this is 2.5 for all channels except the 10.65v GHz channels where it is set to 4.0. The variational Quality Check (VarQC) (Anderson and Järvinen, 1999) weights the data based on the probability of an observation being in gross error relative to the analysis with the weights being recalculated at each iteration of the minimisation.

Scanlon *et al.* (2024) demonstrates that the resultant SKT estimates are realistic and account for known issues, such as the time delay between the background ocean state and the time of the MW observation, for example, by tracking the movement of the Tropical Instability Waves (TIWs). That work was undertaken using the background ocean temperature provided by OCEAN5. The impact of the change to ORAS6 in the context of the SKT estimates derived from MW imagers is discussed in Section 3.

2.3 Assimilating Ocean Observations

In the first minimisation (inner loop) the observations assimilated into the ocean DA system are temperature and salinity profiles from ARGO floats, moored buoys, ships, gliders and sensors on mammals (see Haiden *et al.*, 2018, for further details on these observation types). These are directly provided to

NEMOVAR at the appropriate depths, although some thinning may be implemented where there are multiple observations per model level. Sea Level Anomaly (SLA), which influences the temperature, salinity and currents through the balance operator, is also assimilated in the first outer loop. The SLA sensors active in the current work are: Cryosat-2, Satellite with ARGOS and AltiKa (SARAL), Sentinel-3A and JASON-3.

In the second minimisation, ocean information derived in the atmospheric DA (during its first minimisation) can be passed to NEMOVAR and assimilated. This second ocean minimsation also benefits from atmospheric boundary conditions that have been updated from the first minimisation of the atmosphere. In the current work, in addition to the same ocean observations that were assimilated in the first minimisation, SKT estimates derived from the MW imagers in the atmospheric DA are assimilated into the ocean DA. The ocean is not updated after the second minimisation.

For illustration purposes only (with further discussion later), Figure 2 shows the temperature increments in the top level of the ocean in NEMOVAR (at an average depth of 0.5 m) over a single cycle for (a) the first minimisation, which only benefits from in-situ observations and (b) the second minimisation, where MW imager observations are added. It is clear that the increments from the MW imagers allow more spatially complete information to be provided to NEMOVAR meaning that they can help better constrain the ocean state. This additional spatial coverage is one of the key motivations for the current work.

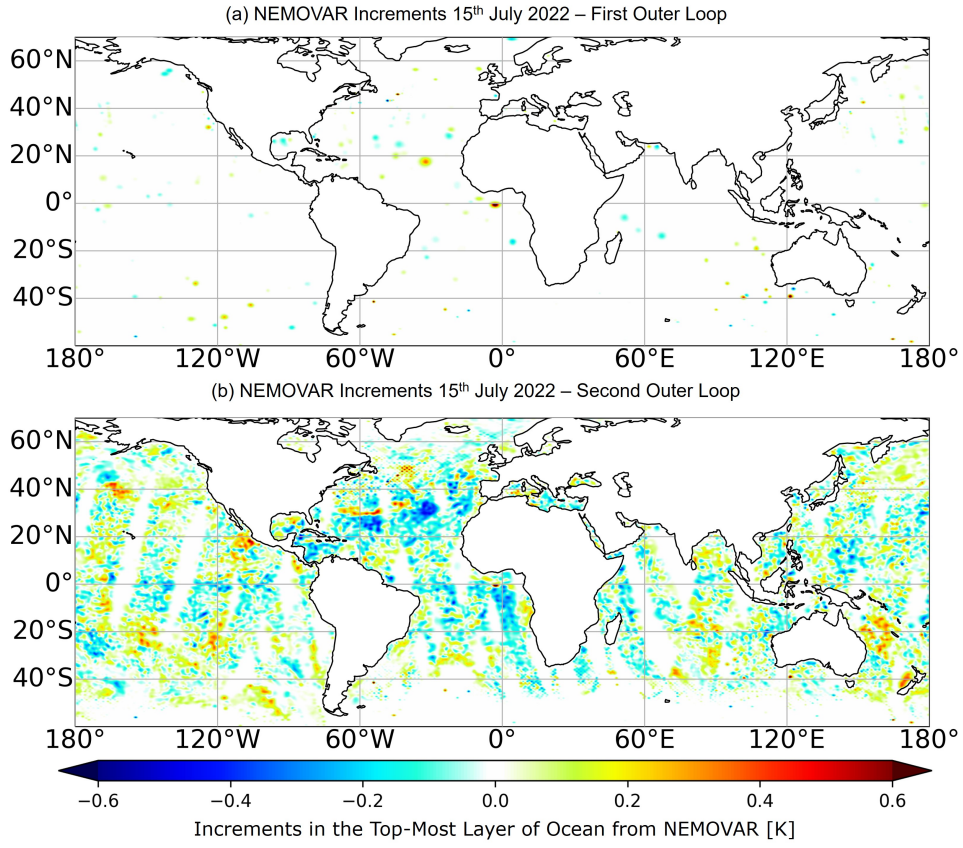

Figure 2: Increments in the top-most level of the ocean from NEMOVAR for (a) the first outer loop of the 2022-07-15 12 UTC cycle which includes in-situ ocean observations and altimeters and (b) the second outer loop which includes the SKT estimates from MW imagers.

The MW SKT observations with model equivalents calculated using the temperature in the top layer

of the ocean and the cool skin parameterisation are assimilated into the ocean using an appropriately linearised version of the model. Further details are provided in Browne *et al.* (2025). The observations are provided to the ocean DA system using an observation error model which is weighted by distance to coastline and a B-matrix which is estimated using a climatology (Chrust *et al.*, 2025). No bias correction is applied to the observations.

For the purposes of the TOVSCV (presented in Scanlon *et al.*, 2024) the quantity representing the temperature in the uppermost layer of the ocean has, thus far, been referred to as SKT as it represents the uppermost layer of the ocean to which observation is sensitive. Due to the penetration depth of MW radiation, in a pure water situation, we would expect the MW SKT to represent a depth of the order of a few millimetres, whereas the ocean's infrared emission is more related to the top 10 microns.

Determining the exact depth of the ocean that the derived SKT represents is challenging for several reasons, including the variability of the ocean both spatially and temporally and the exact data used in the sink variable approach. Figure 3 provides a representation of ocean temperature profiles under different conditions. In this Figure, the skin layer is presented as two distinct regions, the cool skin and sub-skin layers, where Donlon *et al.* (2007) defines the first as the region to which IR channels in the range of 3.7 to 12 microns are sensitive and the second as the region to which MW channels in the range of 6 to 11 GHz are sensitive. Below these layers, the diurnal warm layer is present during the day. Future work will aim to determine the relationship between the SKT observed by the MW imagers and the temperature in the top layer of the ocean model.

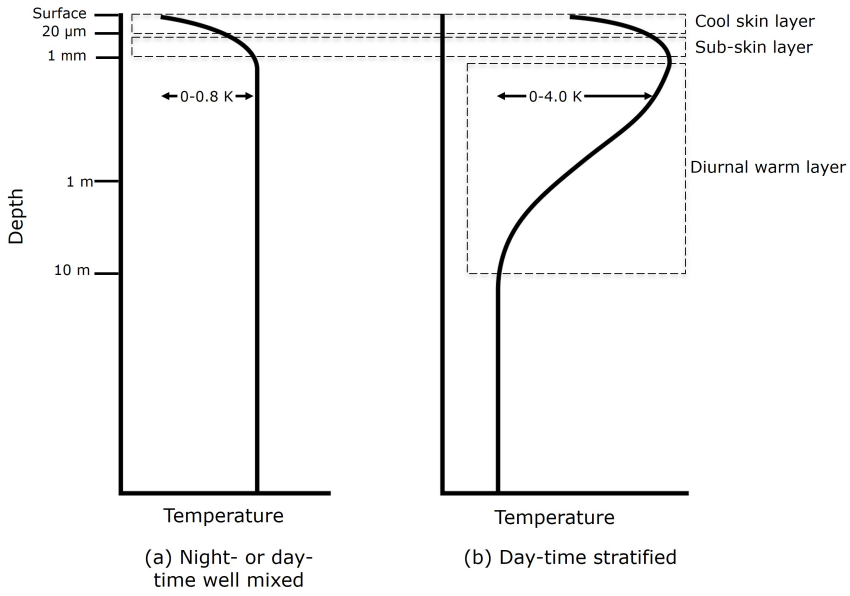

Figure 3: Theoretical upper ocean temperature profiles for (a) night-time or well mixed day-time and (b) day-time during conditions conducive to the formation of a diurnal warm layer, i.e. the vertical portion of the ocean which is subjected to warming as a result of the diurnal cycle. Following Gentemann and Minnett (2008) and using information from Donlon *et al.* (2007).

2.4 Ocean Model and Ocean DA System

Concurrent with the introduction of outer loop coupling, a new ocean reanalysis system, Ocean Reanalysis System 6 (ORAS6) (Zuo *et al.*, 2024), was introduced at cycle 48r2. In ORAS6, ocean observations

are assimilated behind real time to provide a best possible re-analysis. This also provides a background for the near-real-time Ocean Long window Data Assimilation (OLDA) which allows use of newer ocean observations. These systems assimilate a range of ocean observations including temperature and salinity profiles and external Level 3 analyses of the ocean surface temperature, i.e. data products generated from a range of observations.

Previous versions of the IFS atmospheric model obtained their background Sea Surface Temperature (SST) from a combination of Sea Surface Temperature and Ice Analysis (OSTIA) (Good *et al.*, 2020) and OCEAN5 (Zuo *et al.*, 2019) dependent on latitude (ECMWF, 2021; Browne *et al.*, 2019). With the introduction of ORAS6 and ocean coupling, the SST is instead initialised from ORAS6 at 12 UTC every day and then propagated through the DA window and into the forecast by the NEMO model.

The key upgrade in ORAS6 relevant to the current work is that it introduces the direct assimilation of SST information into the ocean model which has been shown to greatly reduce biases in the SST compared to the previously used "SST nudging" (Zuo *et al.*, 2024). In the period considered in this work, the ESA CCI SST v3 (Embury *et al.*, 2024) product is assimilated, noting that after the end of 2023, the OSTIA L4 product from the UK Met Office is assimilated (Donlon *et al.*, 2012; Good *et al.*, 2020).

Another key upgrade in the ORAS6 system is that **hourly** surface forcing from ERA5 is now available to the ocean model and this has resulted in the improvement of the diurnal cycle (Zuo *et al.*, 2024). Therefore, only the cool skin effect (described in ECMWF, 2023) needs to be taken into account within the atmospheric part of the IFS. Note: the cool skin is defined as an approximately 20 microns thick layer (Donlon *et al.*, 2007) where the long wave radiation heat losses to the atmosphere are not compensated for by molecular heat transfer within the water.

2.5 Experimentation

To test the impact that providing ocean information from MW imagers to the ocean DA system has on the IFS, experiments have been run over two seasons (2022-06-01 to 2022-08-31 and 2022-12-01 to 2023-02-14). These experiments have an atmospheric model resolution of TCo399 (29 km) with a final incremental analysis resolution of TL255 (80 km) and 137 vertical levels in the atmosphere. The ocean model used has a resolution of 0.25 degrees and 75 vertical levels (see Section 2.4 for further details).

The background ocean and sea ice in the 12 UTC analysis is provided by an experiment recreating the OLDA (see Figure 1), which is the Near Real Time (NRT) component of the ocean system. This ensures the experimentation represents the operational configuration as closely as possible, in particular the timeliness benefits of being able to use SKT estimates made within the atmospheric DA window, which would not be accessible to the OLDA. The background ocean and sea ice in the 00 UTC analysis is the result of a coupled forecast from the 12 UTC coupled analysis.

Two experiments have been run. The control experiment includes the active assimilation of 6.9 and 10.65 GHz from AMSR2 and 10.65 GHz from GMI with the SKT sink variable activated (see Scanlon *et al.*, 2024). This control experiment assimilates only in-situ and altimeter observations into NEMOVAR, as described in Section 2.4 and shown in Figure 2(a). Building on the control experiment, the second experiment tests the impact of assimilating ocean information derived from the MW imagers into NEMOVAR, as shown in Figure 2(b).

The experiments are run in an LWDA configuration with two cycles per day: the 00 UTC and the 12 UTC cycle. As described earlier, the updated ocean is only provided as the background ocean and sea ice to the 00 UTC window, with the 12 UTC window being reinitialised from the OLDA system to maintain a

constrained ocean. Therefore, although some impact on the 12 UTC cycle is expected due to the updated ocean analysis being used to initialise the coupled forecast, the strongest forecast impact will be seen in the 00 UTC cycle. In the 00 UTC cycle, the background has seen one window of assimilation of AMSR2 and GMI SKT estimates, and the forecast has seen two windows.

The primary metric used in Sections 4 and 5.1 of this report is the change in the ”O-B fit”, i.e the standard deviation of the observations minus the simulated observations based on the background fields. For these ”O-B fit” results, only the 00 UTC cycles are used in the evaluation. For the forecasts results discussed in Section 5.2, both the 00 UTC and 12 UTC cycles are used.

3 Ocean Temperature Increments

3.1 SKT Increments from MW Imagers

Figure 4 shows the increments in SKT generated in the atmospheric DA for two 12 UTC cycles (in July 2022 and January 2023) derived for AMSR2 using the coupled system configuration (panels a and b). In previous work (Scanlon *et al.*, 2024), in an atmosphere only setting, the ocean temperature increments generated through the TOVSCV used a background SST fixed boundary condition taken from a combination of OSTIA and OCEAN5 (dependent on latitude). However, as discussed in Section 2.4, the underlying ocean system has been updated for the current work, and the ocean and sea ice are propagated through the assimilation window by the coupled model. Therefore, Figure 4(c) shows the equivalent increments to panel (a) but generated using the older OCEAN5/OSTIA configuration.

In panels (a) and (b), the increments patterns are similar to those previously discussed for AMSR2 in Scanlon *et al.* (2024) [2], with the most significant feature being the large-scale cooling in the ETP (for both seasons) in the region of TIWs that form along the equatorial cold tongue (e.g. Wentz *et al.*, 2000). These features in the increments have previously been demonstrated to account for deficiencies in the input ocean state and the associated temporal delay between the time at which the observations are taken and the time at which the ocean state is used in the atmospheric DA system. In addition, there is also a warming in the South Pacific Convergence Zone (SPCZ) which has been previously identified (in Scanlon *et al.*, 2024) as a sporadic warming event lasting several days which is not captured in the input ocean state. The only other clear feature shown in these single cycle maps (and also present in the monthly maps) is the warming signal in the North Atlantic which accounts for changes in the position of the Gulf Stream (see Figure 6).

Although in general, the SKT increment patterns are similar between the older atmosphere only system (Figure 4(c)) and the newer coupled system (Figure 4(a)), we do see some differences. In the Gulf Stream, we see that for the newer system, the use of the MW observations result in some large positive increments which were not present in the older system. Part of the work to upgrade to the newer system has considered the repositioning of the Gulf Stream and it appears that the MW observations do not fully agree with this change. The cooling increments in the western boundary currents are less pronounced in the newer system, indicating that the MW observations agree with the changes made in these areas.

Examples of monthly mean increments from the SKT sink variable in the atmospheric DA system for AMSR2 are shown for two seasons (July 2022 and January 2023) in Figure 5 (note those for GMI are not shown here). Note that in Scanlon *et al.* (2024) the increments were shown split by day and night, however here they are shown split by 00 UTC and 12 UTC as it clearly shows those increments which are primarily driving the ocean state (from the 12 UTC cycles) against those which have a lesser impact (from the 00 UTC cycle). These increments show many of the same signals as previously identified in Scanlon *et al.* (2024), for example the persistent cooling in the ETP, the signal potentially caused by dust contamination in July 2022 in the North Atlantic and some warming signals seen in northern latitudes in January 2023.

There are some large differences between the initial ocean conditions derived from the coupled system and the forced atmosphere system (Figure 6(a). For example, there is a large patch of cooler SKT to the south of the Gulf Stream which is likely due to the repositioning of the Gulf Stream in the new

[2]Note: The magnitude of the increments vary between those shown here and those in Scanlon *et al.* (2024) as, due to constraint of working in parallel with the atmospheric DA system, the ocean DA does not have access to the SKT estimates generated from the final minimisation in the atmospheric DA system, only those generated in the first minimisation.

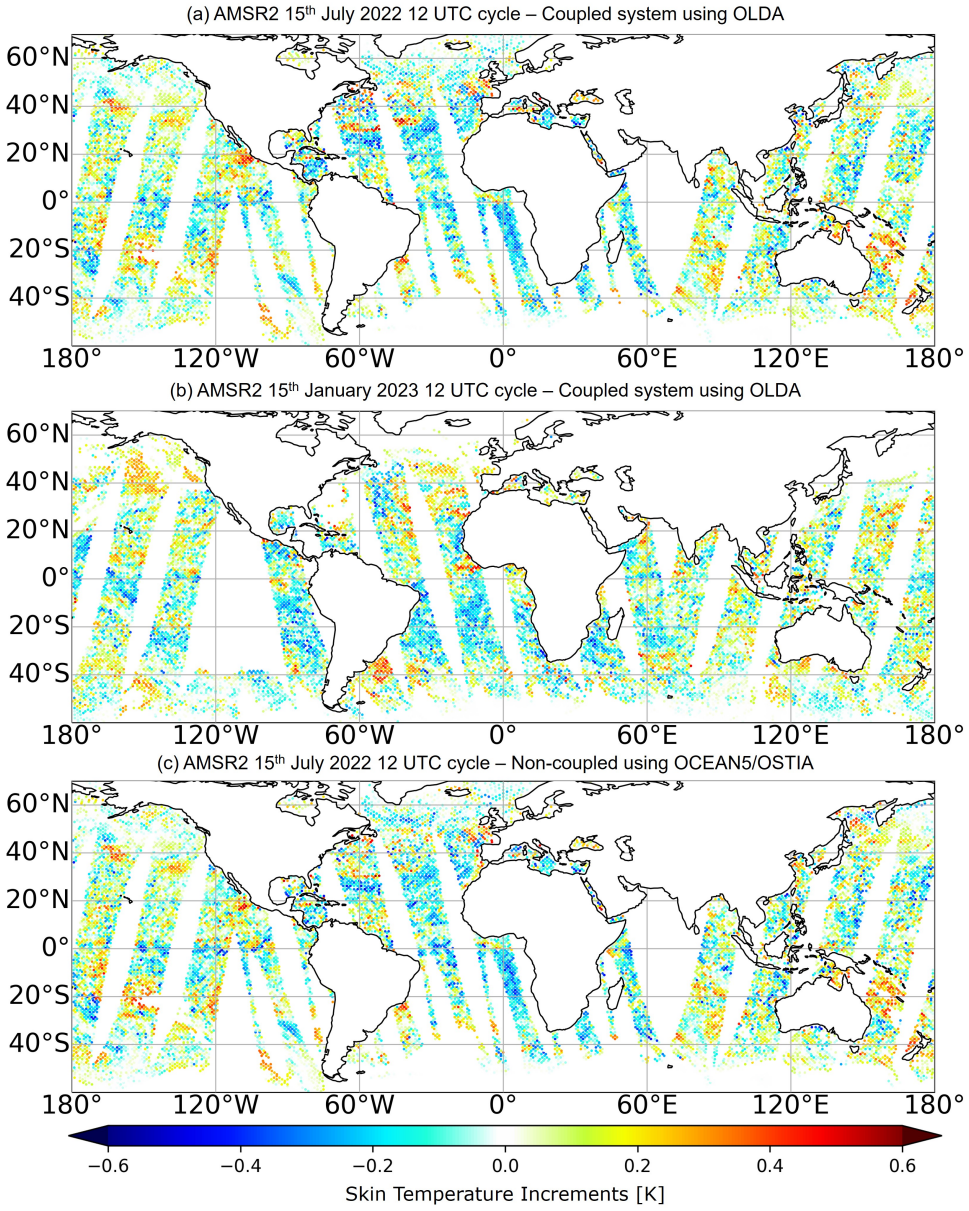

Figure 4: SKT increments generated in the atmospheric DA system for a single cycle of AMSR2 for (a) 2022-07-15 12 UTC window and (b) 2023-01-15 12 UTC window using the OLDA stream available in the coupled system; (c) shows the SKT increments for 2022-07-15 12 UTC window for the previously used, non-coupled system which used information from OSTIA and OCEAN5 as the ocean boundary conditions. The increments shown are only those where the 6.9v GHz channel is available (although a range of channels are used in the generation of the increments).

ocean analysis and there is some cooling of the equatorial currents which is consistent with the results of Scanlon *et al.* (2024) which showed that these currents were too warm.

However, the key point here is that the spatial patterns of the change in the SKT increments between the two systems and the change in the initial conditions have similar patterns but with opposite signs (compare Figure 6a and b). This suggests that the mean increments generated by the sink variable

approach in the earlier system were indicating errors in the OSTIA/OCEAN5 ocean temperature that have been corrected in ORAS6. Hence this provides further evidence that the TOVSCV approach is working as intended.

3.2 Ocean Temperature Increments in NEMOVAR

The SKT estimates derived in the atmosphere DA are passed to the ocean DA system, NEMOVAR. Within this system, the SKT estimates (for both AMSR2 and GMI) are assigned an error of 0.5 K. The 0.5 K error is based on the standard deviation of the observations and then scaled with the large errors historically assigned to in-situ profile (0.78 K at the surface, Ingleby and Huddleston, 2007) observations in order to ensure a balanced system.

Figure 7 shows the increments made in NEMOVAR for each cycle of a single date in July 2022. In these NEMOVAR increments, the swath patterns of both GMI and AMSR2 are clearly visible. The wide AMSR2 swaths can be seen, for example, over the Pacific in both cycles and the thinner GMI swaths can be seen, for example, to the east of Africa in panel (a) and to the south of India in panel (b).

A significant feature seen in the NEMOVAR increments is the difference between the regions of the Earth where it is day-time and night-time. For the 12 UTC cycle (panel a) it is day-time over the Atlantic and for the 00 UTC cycle (panel b) it is day-time over the Pacific. The increments during the day-time generally have a strong preference for cooling increments.

There are a few geographical areas in these single cycle maps of NEMOVAR increments where spotted patterns are apparent, as shown in Figure 8. This is likely a result of the relative sparseness of satellite observations compared to the NEMO model grid. The error correlation length scales in NEMOVAR are specified using a diffusion operator (Chrust *et al.*, 2025), and for temperature in the top most layer of the ocean they are intentionally short due to the high variability in these regions. These short length scales are necessary to prevent the observation of one geophysical feature (for example the main current of the Gulf Stream) influencing other geophysical features close by (for example the Gulf Stream 'rings' which are large scale (100 - 300 km) eddies of cool water which form to the sides of the main current). However, this also means that the length scales are shorter than the distance between the superob locations of AMSR2 and GMI, which are driving the NEMOVAR increments. Although the superobbing resolution is approximately 40 km, a 1 in 8 thinning has also been applied for atmospheric data assimilation in order to achieve a 110 km distance between actively assimilated superobs. The 'spottiness' of the NEMOVAR increments could be addressed through the use of the 'surface-only' observations of the SKT from AMSR2 and GMI discussed in Scanlon *et al.* (2024) if appropriate modifications were made to ensure these additional observations do not overwhelm the atmosphere DA system or if these additional observations are used only in specific geographical regions such as those shown in Figure 8.

Figure 9 shows the increments made within NEMOVAR aggregated by month for the 00 UTC and 12 UTC cycles as a result of passing the SKT estimates derived from AMSR2 and GMI observations to the system along with the in-situ and altimeter data. It can be seen that the patterns are similar to those shown for AMSR2 in Figure 5. The patterns are also similar to the monthly means of the SKT increments from GMI (not shown). The monthly increments from NEMOVAR (Figure 9) are of a lower magnitude than those generated by the sink variable approach in the atmospheric system for individual sensors (e.g. Figure 5) due to the use of observation errors which affect the influence that individual observations have on the ocean DA system.

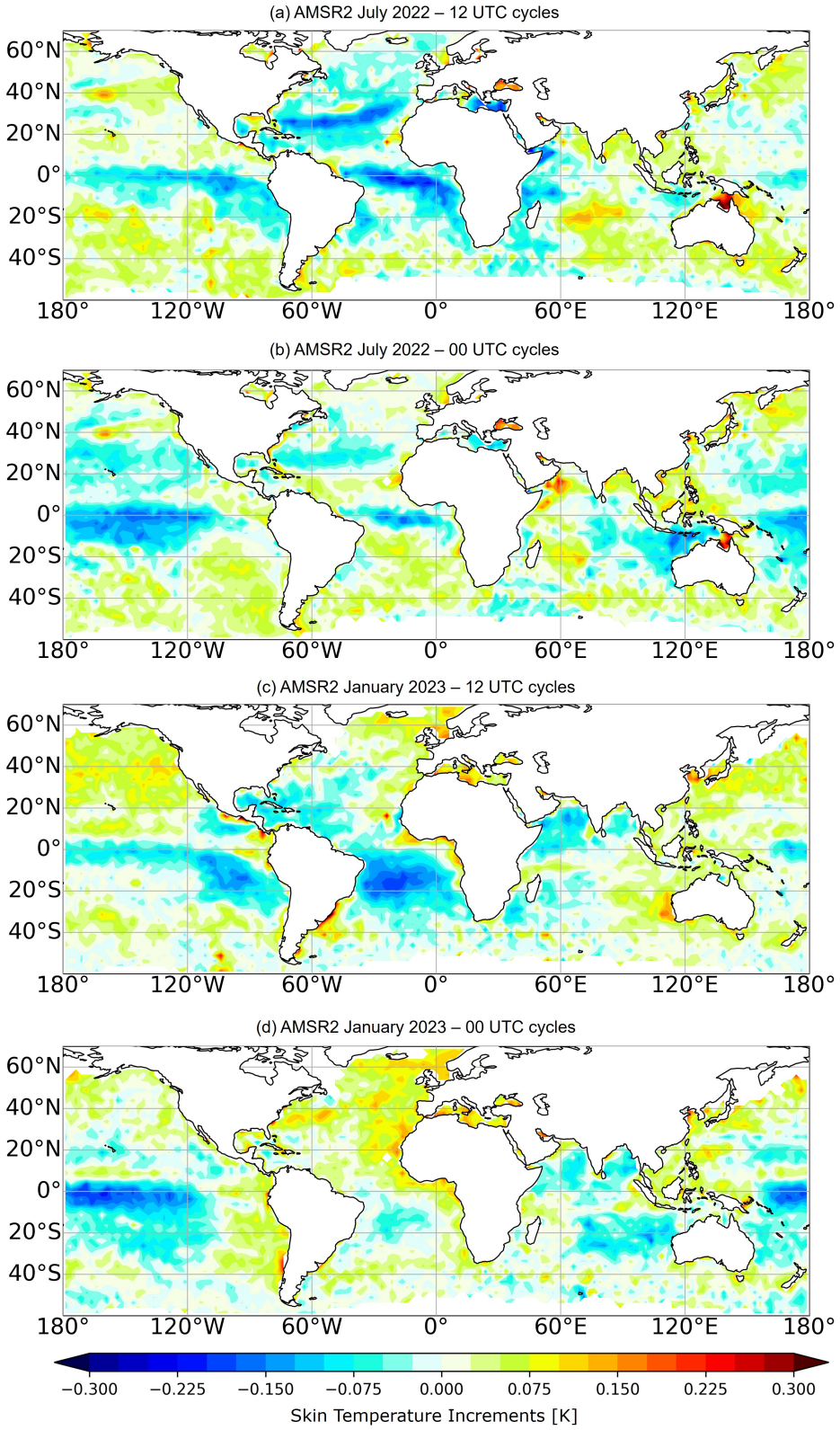

Figure 5: Monthly means of SKT increments generated in the atmospheric DA system for AMSR2 for the dates indicated split by the 12 UTC and 00 UTC cycles. The increments shown are only those where the 6.9v GHz channel is available (although a range of channels are used in the generation of the increments).

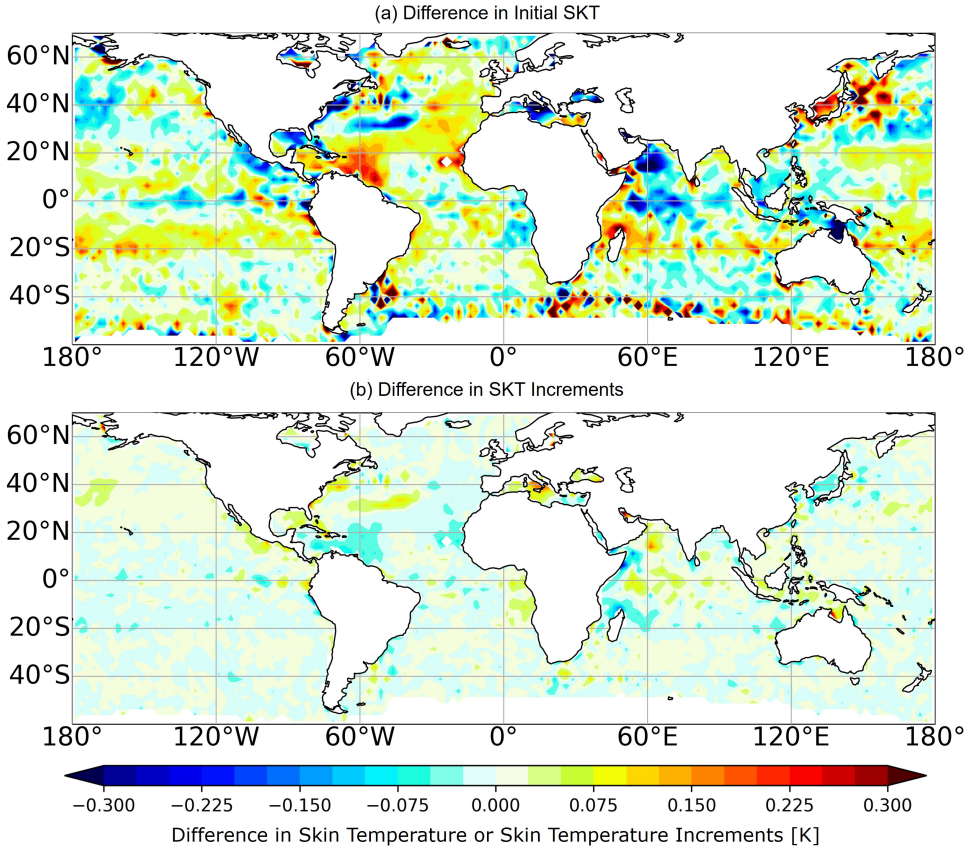

Figure 6: Difference between (a) the SKT derived from the initial ocean conditions provided by the coupled system and the forced atmosphere system and (b) difference in the resulting SKT increments generated through the TOVSCV approach in the atmospheric DA system for AMSR2 2022-07-01 to 2022-07-31 for the 12 UTC cycles.

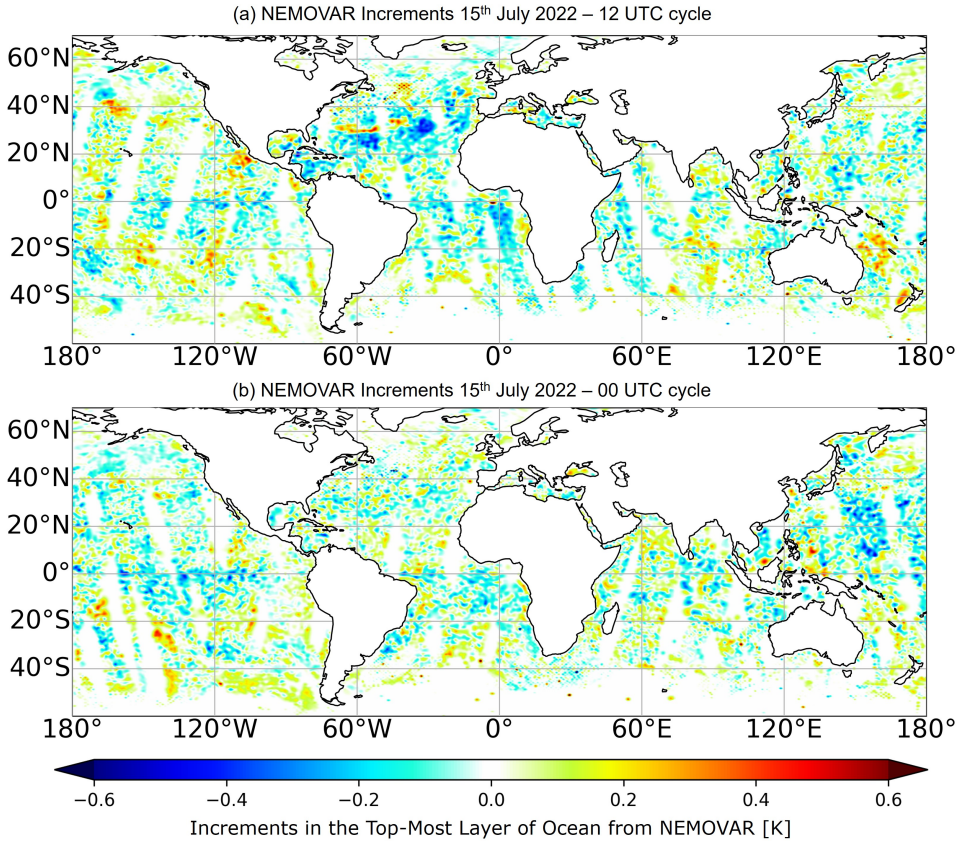

Figure 7: Single cycle NEMOVAR increments in the top-most level of the ocean for the 15th July 2022 for the 12 UTC and 00 UTC cycles.

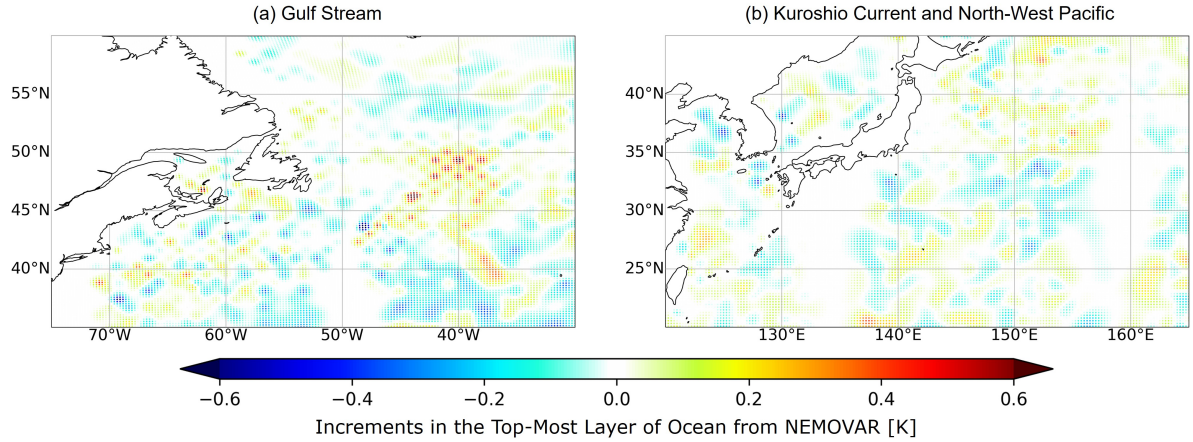

Figure 8: Single cycle NEMOVAR increments in the top-most level of the ocean for the 15th July 2022 for the 12 UTC cycle for (a) the region around the Gulf Stream and (b) the Kuroshio current and North West Pacific.

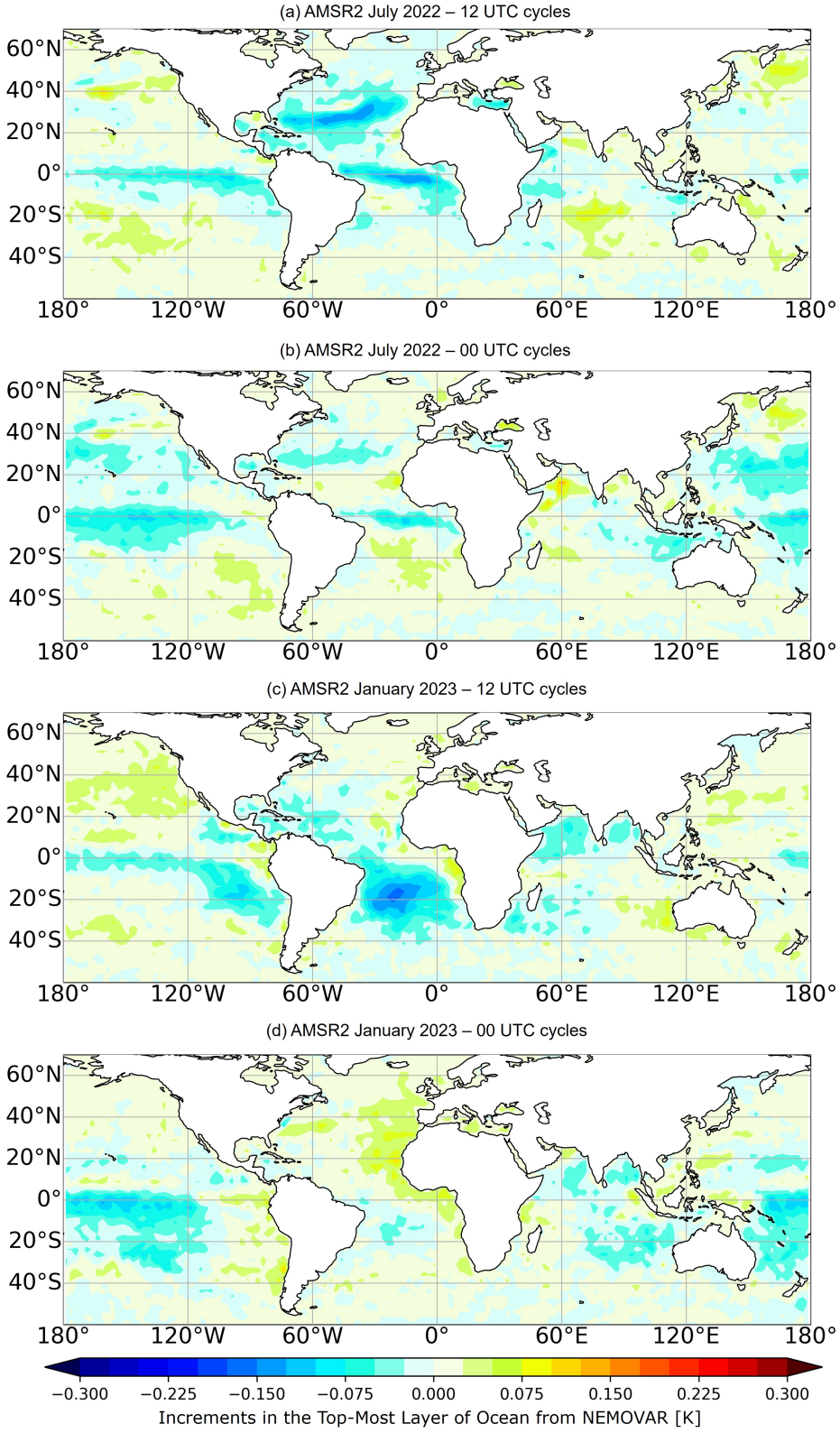

Figure 9: Monthly means of NEMOVAR increments in the top-most level of the ocean for the dates indicated split by the 12 UTC and 00 UTC cycles.

4 Evaluation of the Impact on the Ocean System

4.1 Using ARGO Float Observations

The coupled ocean DA system provides the ocean temperature at 75 vertical levels (Zuo *et al.*, 2024) with varying vertical resolutions. These temperatures can be compared with in-situ ocean temperature profile observations which have been assimilated into the coupled DA system. This section considers the model fits (i.e the standard deviation of the BG departures) to understand the benefit gained from assimilating the SKT estimates derived from the MW imagers into NEMOVAR. Note that, as discussed in Section 2), only the changes in the 00 UTC cycle will be presented here, as the ocean has only been influenced by the AMSR2 and GMI SKT estimates in the background of the 00 UTC cycle and not the 12 UTC cycle.

In this analysis only the ARGO floats are used due to their superior temporal and spatial coverage over other in-situ observations available during the study period. ARGO floats (Wong *et al.*, 2020; Roemmich *et al.*, 2019; ARGO, 2025) are an array of instruments which take profile measurements of the ocean from the lowest depth (either 2000 m or the seafloor (Zilberman *et al.*, 2023)) upwards by inflating an external bladder (e.g. Morris *et al.*, 2024). Currently, there are about 3000 ARGO floats that provide 100,000 profiles of ocean observations per year with an average spacing of 3 degrees (ARGO, 2025) (see Haiden *et al.*, 2018, for the spatial distribution of the floats used within the ECMWF system). This relatively high data volume, combined with the high quality of the observations (e.g. Wong *et al.*, 2020; Johnson *et al.*, 2022; Morris *et al.*, 2024) makes the ARGO float dataset crucial for ocean studies (as discussed for various applications in Johnson *et al.*, 2022).

Whilst there are known issues with the salinity measurements taken by ARGO floats (See Roemmich *et al.*, 2019; Johnson and Fassbender, 2023, for further details), no documented issues with the temperature profiles have been found during the review of the literature carried out for the current work. However, there is still a need to ensure the ARGO float data being used here are of the best quality.

There are two levels of Quality Control (QC) implemented for the ARGO floats: the automatic QC implemented for NRT observations and the Delayed Mode QC (DMQC) implemented when the data is distributed with a delay of up to 12 months which includes assessing the shape of the ARGO temperature profiles (Wong *et al.*, 2024; Morris *et al.*, 2024; Zilberman *et al.*, 2023). At ECMWF, the NRT data stream for the ARGO floats is used, as the data are made available within 24 hours of upload from the float to the communication satellite (Morris *et al.*, 2024). These data have some QC procedures applied (as outlined in Morris *et al.*, 2024; Wong *et al.*, 2024) with the QC flag meanings listed at NERC (2025). In some studies (e.g. Roemmich and Gilson, 2009; Tan *et al.*, 2023), additional QC is applied when the NRT data is used, to ensure robust results, with recent work focussing on the application of ML techniques (e.g. Sugiura and Hosoda, 2020; Sui and Jiang, 2024).

Within the IFS, the ARGO float data is not subject to bias correction or VarQC, however, the checks detailed in Good (2008) are applied; as this document is not available to the public, the QC checks are summarised here, with further relevant information on similar checks available in Tan *et al.* (2023):

- Profiles from ARGO floats listed in a ”greylist”, which are deemed bad data, are rejected.
- The automated quality control flags provided with the NRT data are used to reject those data flagged as ”bad” or ”probably bad”.
- Temperatures below 269.15 K and above 313.15 K are rejected.

- Temperature profiles are checked for occurrences of constant values, spikes and steps and those profiles with a certain percentage of observations affected by these issues are rejected.
- The data is horizontally thinned to ensure a 25 km spacing and a temporal gap of 24 hours.
- Profiles are checked for density inversions (i.e. the density of the water is not increasing with depth), and if a certain percentage of observations are flagged within a profile, the profile is rejected.
- Profiles within a certain distance of a coastline are rejected.

For the use of the ARGO observations in the assessment of the BG departures presented in this section, further QC is applied in addition to those already applied in the IFS. The observation temperature in the top two meters of the ocean is checked and if it is less than 280 K, the whole profile is rejected to ensure the observations are taken in open ocean rather than close to sea ice. If there are 10 observations or less in a profile or the maximum depth of the profile is less than 250 m the whole profile is rejected which helps to reduce outliers in the data.

Some recent work has focused on the identification and rejection of profiles where the shape deviates from that expected from knowledge of the physics of the ocean (e.g. Tan *et al.*, 2023), for example, where the top level of the ocean appears much colder than the water beneath. In the current work, some of these profiles are excluded through the methods detailed above; however, many such profiles remain. To address this here, we use the correlation between the model temperature and the observations, where the model temperature is controlled through knowledge of the physics of the ocean. Calculating the correlation in the top 500 m and excluding profiles where the correlation is less than 0.8 allows for many of these deviating profiles to be excluded.

After applying the above QC checks, the ARGO float data is binned to the NEMO model levels. For the model levels from 10 m depth to the lowest depth, the original bins are kept, however for those above, they are aggregated into two bins of 2.25 m (covering the top 4.5 m of the ocean) and then one bin of 4.5 m (covering from 4.5 m to 9 m). The aim of re-binning these top bins is to provide a similar number of ARGO float observations in each bin as above 10 m depth the ARGO floats provide much sparser data than below.

Due to the nature of in-situ observations (temporally and spatially sparse), the results presented in the following sections highly depend on the aggregation applied in terms of depth, the specific geographic area and time period. To ensure the results presented here are robust to these issues, the longest possible time periods have been used along with large geographical areas. This is to increase the number of data points available and hence reduce the potential variability of results.

It should be noted that the analysis of the fits of the ARGO floats presented here cannot be considered a fully independent validation of the method. This is because the ARGO floats are being used in both the generation of the updated ocean and the validation. Therefore, there will be some preference of the system to these observations, likely through common sensor characteristics. i.e. systematic biases, and through sampling and representation errors (i.e. the same errors are being made in both datasets).

However, some independence is achieved through the choice to use only the ARGO float observations from the 00 UTC cycle in the comparison of the BG departures presented here. The ARGO floats from the 12 UTC cycle which are used to create the updated ocean, which is then used as the background for the 00 UTC cycle, are not used in the comparison.

To achieve a fully independent validation, the in-situ observations used should not inform the ocean

model at all, however, there are very few high-quality observations available which meet this criteria. Therefore, the fit of the in-situ ocean observations to the model are considered an indicator of the benefit gained from including the SKT estimates from MW imagers into the coupled system.

4.2 Impact on the Fit to ARGO Float Observations

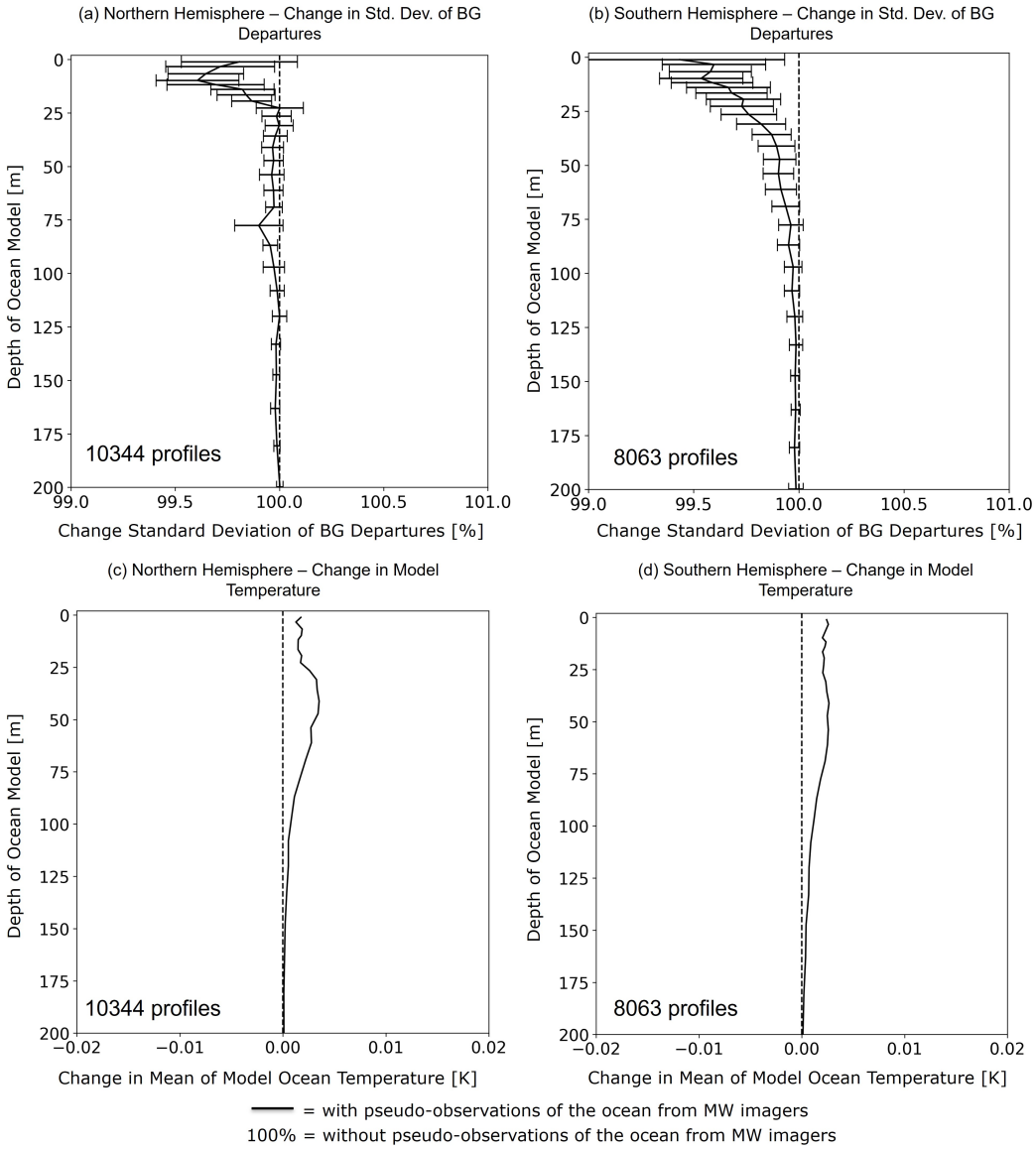

Figure 10: Relative change in the standard deviation of the BG departures (a and b) and the model temperature (c and d) from ARGO floats for the 00 UTC cycle. For the Northern Hemisphere (a and c) and the Southern Hemisphere (b and d) for the period 2022-06-07 to 2022-08-31 and 2022-12-07 to 2023-02-14 for the 00 UTC cycles.

Figure 10 shows the relative change in the standard deviation of the background departures for the ARGO floats and the change in the ocean model temperature split by hemisphere, with the Northern Hemisphere defined as 20 °N to 70 °N and the Southern Hemisphere defined as 20 °S to 60 °S to avoid sea-ice con-

tamination. Each plot shows the top 200 m of the ocean as this is the range in which the most impact is made from adding the SKT estimates derived from MW imagers to the ocean DA system. The number of profiles on which the data is based is provided on each plot.

In both the northern and Southern Hemispheres, the addition of the MW observations leads to a slight warming of the ocean in the top 150 m at the locations of the ARGO floats. In terms of the fit (standard deviation) of the background departures, for the Northern Hemisphere we see statistically significant improvements in the first 25 m (with the exception of the top-most bin) and in the Southern Hemisphere the statistically significant improvements extend down to around 75 m.

The error bars in Figure 10(a and b) reflect the day-to-day variability associated with the ARGO float observations. Due to their sparse nature, it is possible that there are some days where a single ARGO profile could have a large impact on the magnitude of the error bars. However, for the plots shown in Figure 10, no such occurrences could be identified and therefore, the error bars shown here are considered to represent the natural variability associated with a sparse dataset.

Due to the availability of a significant number of the ARGO observations in the region, we have the opportunity here to revisit the Eastern Tropical Pacific (ETP). In this area, the NEMOVAR increments show a strong cooling of the ocean with the increments showing a pattern reminiscent of Tropical Instability Waves (TIWs). this is shown in Figure 11 which is a close up of the ETP from Figure 9(a and b). Scanlon *et al.* (2024) demonstrated that these increments are related to the time delay between the input SST products and the time of the microwave observations. As can be seen from Figure 11, increments in this area are strongest in the 00 UTC cycle (panel b), however, as previously discussed, the background ocean state is only updated from the increments made in the 12 UTC cycle (panel a) and therefore, the majority of the impact in this region is not represented in the background departure statistics.

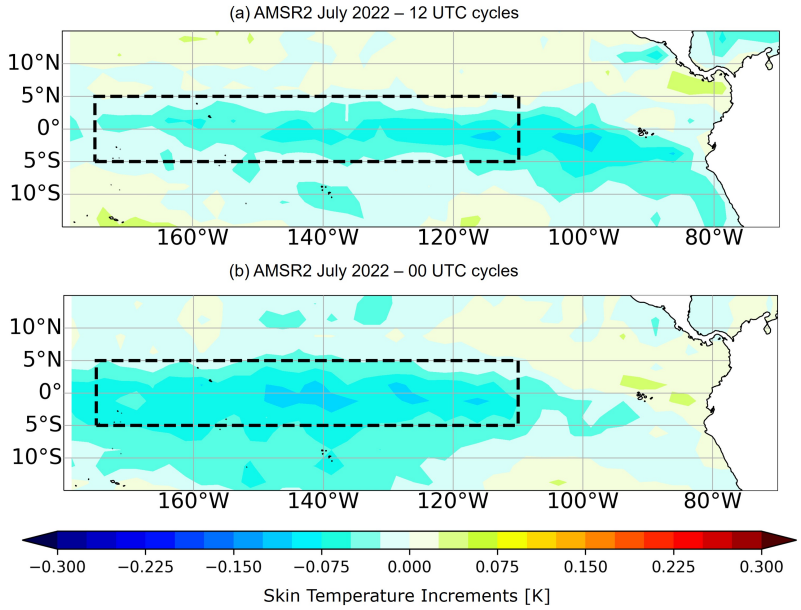

Figure 11: Monthly means of NEMOVAR increments in the top-most level of the ocean for 2022-07-01 to 2022-07-31 for (a) 12 UTC cycles only and (b) 00 UTC cycles only over the Eastern Tropical Pacific where Tropical Instability Waves are observed.

Figure 12 shows the impact that the changes in the ocean have in the ETP in terms of the fit of ARGO float departures (panel a) and the model temperature at the ARGO float locations (panel b). The ARGO

floats suggest that the background is overall in better agreement with observations in this area when the SKT information is added, as shown through reduced standard deviations of background departures of up to 4% (Figure 12(a)). This highlights an improvement in the short-range ocean forecast. The changes in the mean temperature at the ARGO locations are overall very small (around 0.02 K, Figure 12(b)). It is noted that the error bar for the top-most bin near the surface of the ocean is very large ($\pm$46%) which is due to the small number of data points available in this bin (about 200 observations compared with a mean of around 3000 observations for the remaining depth bins shown).

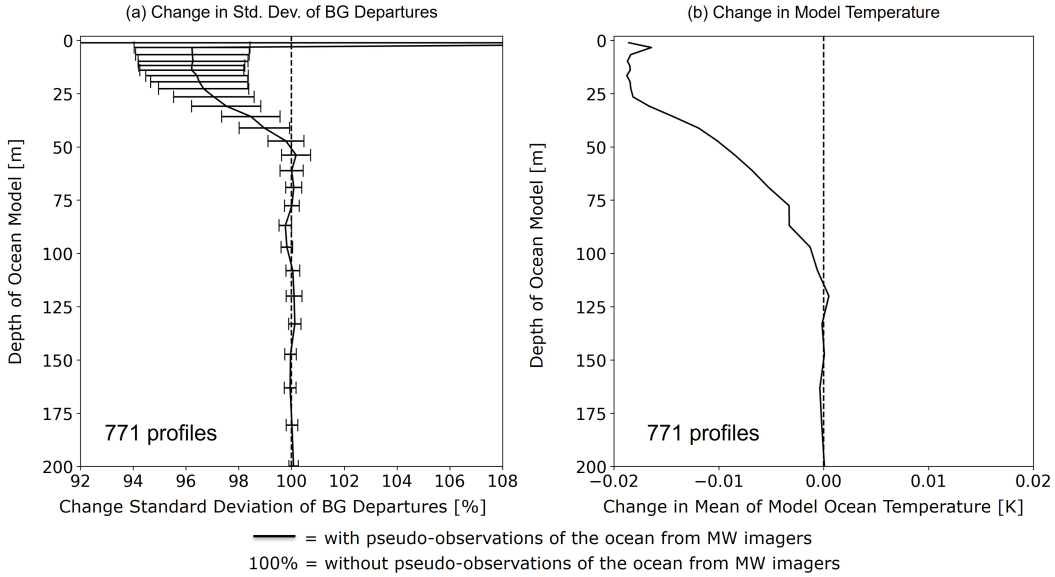

Figure 12: Relative change in the standard deviation of the BG departures (a) and the model temperature (b) from ARGO floats. For the Eastern Tropical Pacific for the period 2022-06-07 to 2022-08-31 and 2022-12-07 to 2023-02-14 for the 00 UTC cycles.

In the Mediterranean Sea, the increments generated in the ocean in NEMOVAR vary strongly between the two seasons studied with widespread cooling in July 2022 and warming in January 2023. It is unclear why this is the case, however it may be related to the marine heatwave experienced in the Mediterranean in 2022 (Pirro *et al.*, 2024). Another potential reason might be that the generation of the updated SKT in the atmospheric DA is affected by the salinity being set to a constant of 35 PSU globally when it is known that the Mediterranean has a higher salinity.

4.3 Impact on Significant Wave Height

At ECMWF, waves are represented by a stand-alone model which is weakly coupled to the ocean model. As part of this wave model, variables such as Significant Wave Height (SWH) are derived. The use of SKT estimates from MW imagers in the coupled system also improves the agreement of the model background with SWH, indicating an improved short-range wave forecast. Figure 13 shows that for two of the instruments (SARAL and CYROSAT-2) there are statistically significant reductions in the standard deviation of background departures. There is no particular geographical pattern associated with these improvements and therefore it is thought that these are a result of the general improvements in the representation of the ocean or the atmosphere.

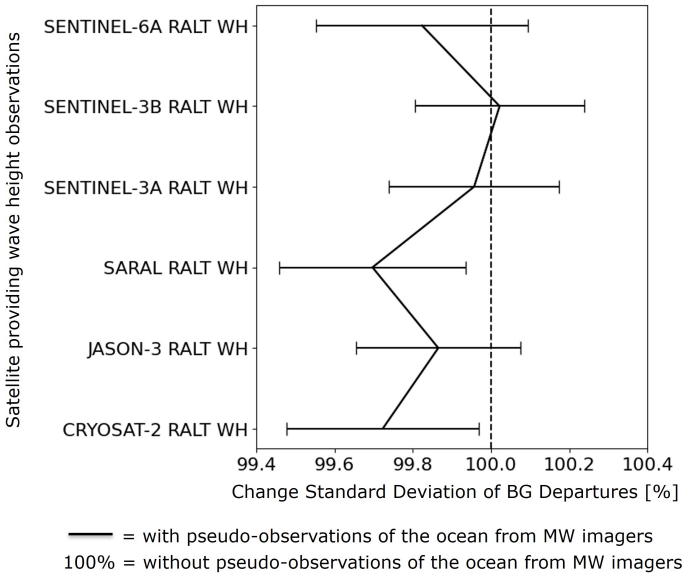

Figure 13: Relative change in the standard deviation of the BG departures for SWH observations. For the tropics for the period 2022-06-07 to 2022-08-31 and 2022-12-07 to 2023-02-14 for the 00 UTC cycles.

5 Impact on the Atmosphere

5.1 Impact on Atmospheric Background Departures

The impact of the updated ocean on the atmosphere is assessed in this section in terms of the change in the standard deviation of the BG departures between the control and the experiment where the SKT estimates are used to inform the coupled model. Note that, as discussed in the Method section (Section 2), only the changes in the 00 UTC cycle will be presented here as the updated ocean is only seen by the background of the 00 UTC cycle, whereas for the 12 UTC cycle the background is reinitialised from the input ocean data stream.

As part of recent development at ECMWF, the windows channels on-board geostationary satellites are now actively assimilated in the atmosphere DA system. These include the 10.3 microns channel from ABI (on-board GOES 16, 17 and 18), the 10.3 microns channel from AHI (on-board Himawari-8 and -9) and the 10.8 microns channel (on SEVIRI on-board Meteosat 9, 10 and 11).

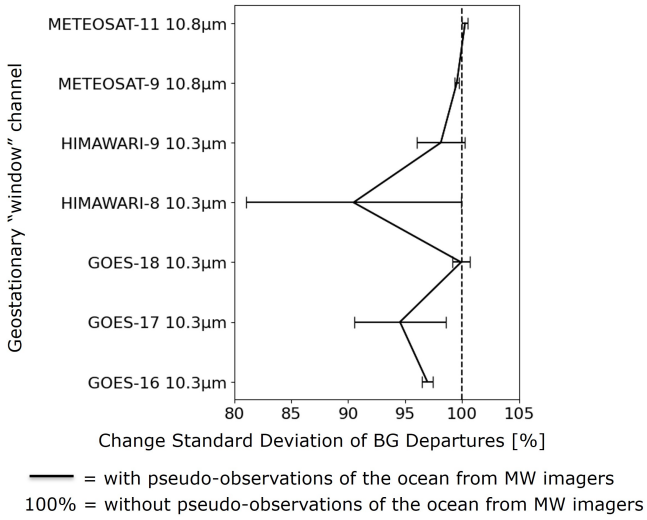

Figure 14: Normalised change in the standard deviation of BG departures for the 10.3 microns channels on-board GOES-16, -17 and -18 and HIMAWARI-8 and -9 and the 10.8 microns channels on-board Meteosat-9 and -11. Global statistics for the period 2022-06-07 to 2022-08-31 and 2022-12-07 to 2023-02-14 for the 00 UTC cycles.

The change in the standard deviation of the BG departures for the window channels is shown in Figure 14. The largest and statistically significant changes are for HIMAWARI-8 (positioned at 140.7 °E, GOES-17 (positioned at 137.2 °W, and only available until 2023-01-04) and GOES-16 (positioned at 72.5 °W).

Figure 15 shows the changes in the standard deviation of the BG departures over the whole time period for all geostationary satellites with the window channels listed in Figure 14. There are strong improvements in the Eastern Pacific near the coast of South America (in the region of the stratocumulus to cumulus transition associated with the Andes), to the south of Australia and near the coast of Russia in the North Pacific (near to storm-track regions).

For all other atmospheric observations, the standard deviation of background departures is mostly not statistically significantly changed. This is a positive aspect, as it indicates that the considerable changes made to the ocean state do not negatively affect short-range atmospheric forecasts.

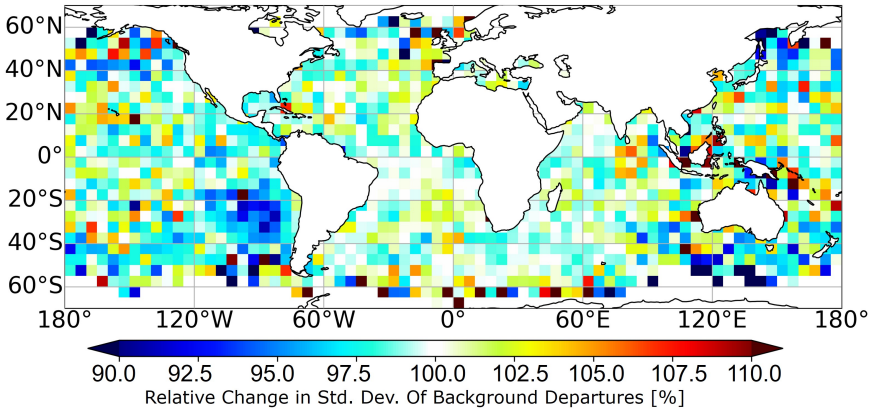

Figure 15: Map of normalised change in the standard deviation of BG departures for the 10.3 microns channels on-board GOES-16, -17 and -18 and HIMAWARI-8 and -9 and the 10.8 microns channels on-board Meteosat-9 and -11. Global statistics for the period 2022-06-07 to 2022-08-31 and 2022-12-07 to 2023-02-14 for the 00 UTC cycles.

The changes in the ocean background at 00 UTC are directly influenced by both AMSR2 and GMI observations from the 12 UTC assimilation window. Therefore, the resultant changes in the BG departures for these observations are not independent and cannot be considered a reliable representation of the system performance. However, they can be used to demonstrate that the system is working as expected and therefore, we show these results here in Figure 16.

As can be seen from Figure 16, the majority of the changes for the MW imager channels are neutral. The largest changes are the improvements in the 6.9v GHz channel on-board AMSR2 (about 0.5%) which is statistically significant and the 10.65v GHz channel on GMI, which is very close to being statistically significant. These channels are highly sensitive to the surface (Scanlon *et al.*, 2024) and the AMSR2 6.9v Ghz channel is the main source in terms of the magnitude of the SKT increments (see Section 3 and Scanlon *et al.* (2024)). Therefore, it is expected that the updated ocean at 12 UTC will lead to a significant improvement in the fit of the BG departures at 00 UTC as has been demonstrated for the geostationary window channels above.

These changes in the BG departures for AMSR2 and GMI demonstrate that the ocean is being updated in line with the information provided by these observations. While it is likely that there are still some biases between the updated ocean state and the truth (considered against somewhat independent observations in the comparison to ARGO floats in Section 4), the updated ocean is providing a better boundary condition for the use of the AMSR2 and GMI observations, to which the lower frequency channels are sensitive.

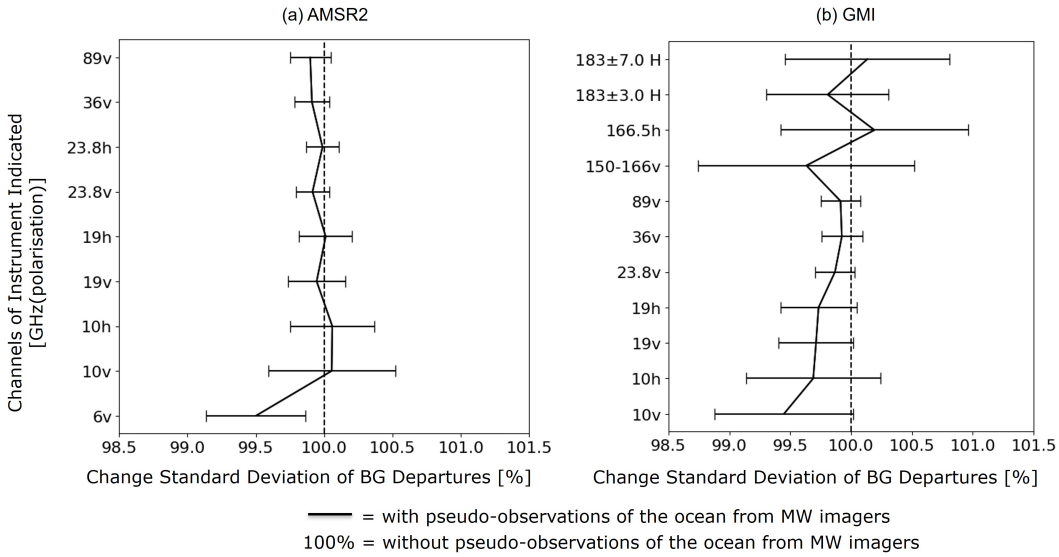

Figure 16: Normalised change in the standard deviation of BG departures for MW imagers due to using the MW ocean information in the coupled system. Global statistics for the 00 UTC cycles for the period 2022-06-07 to 2022-08-31 and 2022-12-07 to 2023-02-14.

5.2 Impact on the Coupled Forecast

The addition of SKT estimates from MW imagers to the coupled DA system has been demonstrated thus far to have a range of impacts on both the ocean and atmospheric observations. In this section, we consider the impact of this change on the coupled forecast. The forecast scores and mean changes presented here are those generated from both the 00 UTC and 12 UTC cycles.

To assess the change in the quality of forecasts, statistics such as RMSE and standard deviation are calculated between the forecast and the own-analysis which is assumed to be the best estimate of the true atmospheric state. This is done for each experiment, i.e. the control and the experiment where the SKT estimates from MW imagers are passed to the coupled DA system and the results compared. Further information on the calculation of these statistics is provided in Geer (2016).

In terms of mean forecast fields, the most notable changes are in the SST as shown in Figure 17. Strong cooling pattens are apparent in equatorial regions which are also present in the ocean DA increments (Figure 9) and the SKT increments derived in the atmosphere DA (Figure 5). These patterns persist over time (shown here up to T+168h, i.e 7 days) illustrating that the SKT estimates from the MW imagers are having a large and lasting, albeit small, impact on the SST field in the forecast.

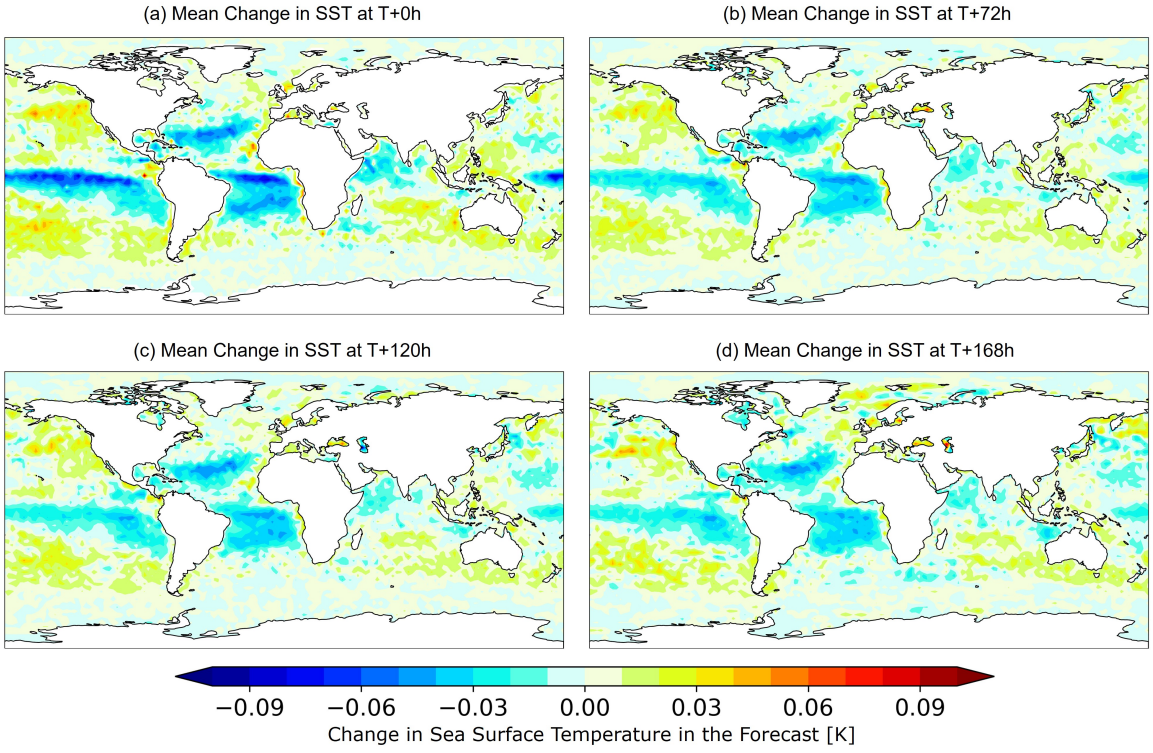

Figure 17: Change in the mean SST forecast field at the forecast times indicated. Global statistics for the period 2022-06-07 to 2022-08-31 and 2022-12-07 to 2023-02-14 for the 00 UTC and 12 UTC cycles.

Changes similar to the changes in SST are also seen in the 2 m temperature (not shown) and in the air temperature both in terms of spatial extent and magnitude, implying that these changes are having a direct impact on the atmosphere. This is shown for one forecast step, T+72h, in Figure 18 for 1000 hPa (panel a) and 925 hPa (panel b), demonstrating that these spatial patterns persist up through the atmosphere.

Figure 18(c and d) show the normalised change in the RMSE of the temperature forecast field. At

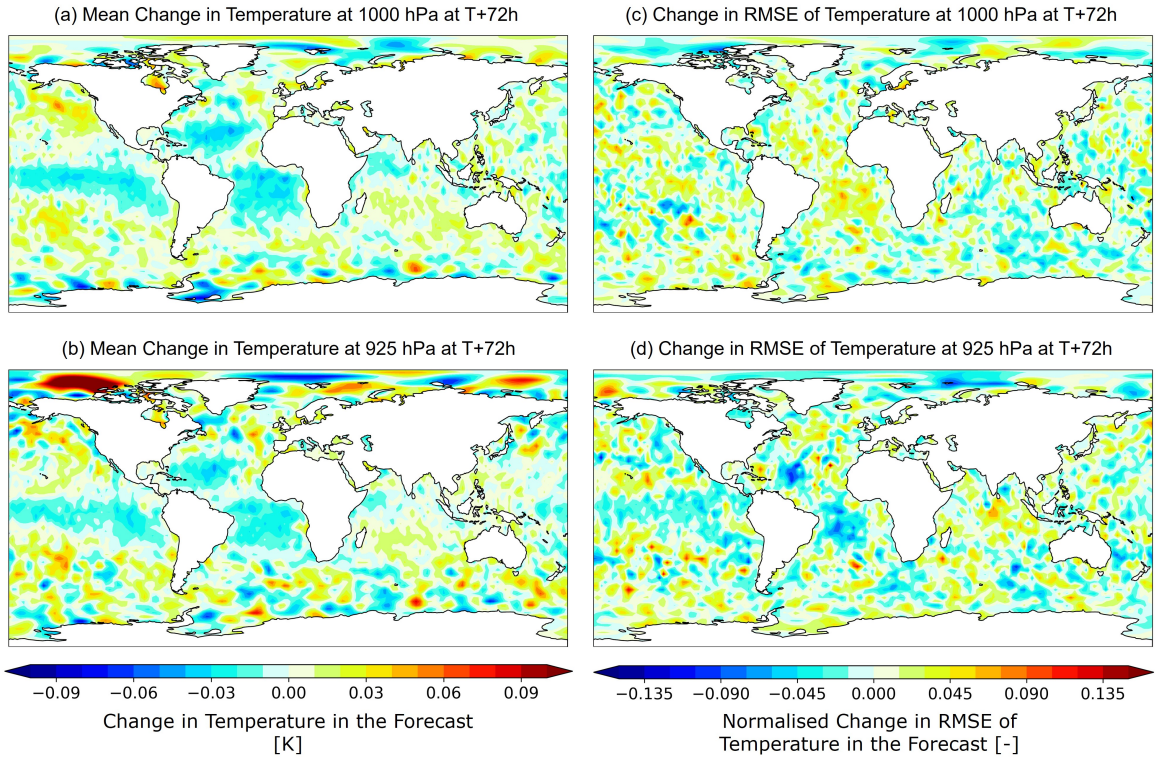

Figure 18: Change in (a and b) the mean air temperature forecast field and (c and d) the normalised RMSE at T+72 hours for the pressures indicated. Global statistics for the period 2022-06-07 to 2022-08-31 and 2022-12-07 to 2023-02-14 for the 00 UTC and 12 UTC cycles.

the surface (1000 hPa in panel c) there is some reduction in the RMSE particularly in the Southern Hemisphere and around the tropics near Indonesia. However, there is also some increase in the RMSE in the tropics and subtropics between South America and Africa, which is a region where the ocean is being strongly cooled by the addition of ocean temperature information from MW imagers. At 925 hPa, the RMSE improvements start to more strongly mimic the changes in the oceans, with large improvements seen around the tropics both in the region degraded at 1000 hPa (between South America and Africa) and in the region of the TIWs (previously discussed in Section 4.2).

The change in the RMSE of the temperature is shown as latitude-pressure plots for 4 forecast times in Figure 19. While the T+24 hour forecast (panel a) shows little change in the RMSE, by T+72 hours (panel b) the RMSE is showing statistically significant reductions in the RMSE over the Southern Hemisphere up to 100 hPa (denoted by hatching and discussed further later). Panels (c) and (d) show that at subsequent forecast times, the general pattern of improvements continues; however, the statistically significant areas appear in other locations. This illustrates that the changes made to the use of SKT estimates from MW imagers takes several days to impact the forecast system. This is likely due to the longer timescales on which the ocean operates compared to the atmosphere.

The benefit for medium-range forecasts is also notable in hemispheric scores, with most statistically significant improvements occurring around T+96h (e.g., Figure 20). For relative humidity, the largest statistically significant change is at the surface (1000 hPa) over the tropics. Here, we see a consistent statistically significant signal from days 2 to 8. Note that these improvements are seen in both seasons (JJA 2022 and DJF 2022/3), with a slightly larger improvement being present in DJF 2022/3 than JJA

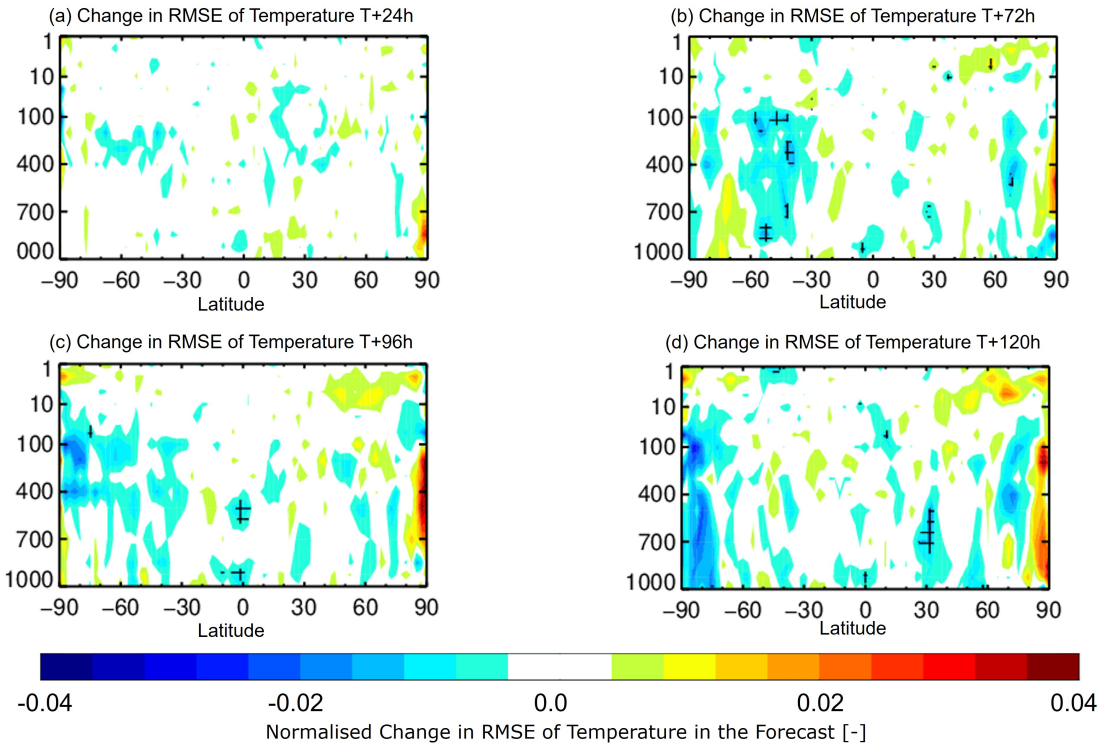

Figure 19: Change in the normalised RMSE of air temperature at the forecast times indicated. Global statistics for the period 2022-06-07 to 2022-08-31 and 2022-12-07 to 2023-02-14 for the 00 UTC and 12 UTC cycles. Note that the cross-hatching indicates point statistical significance at 95% as described in Geer (2016) (**?**).

2022. The improvements for relative humidity at 1000 hPa are investigated further in Figure 21, highlighting that the reductions in the RMSE for the 48h forecast coincide with increases in the mean relative humidity (panel a).

Indications of upward propagation of the changes in the atmosphere are also highlighted in Figure 21. It can be seen that the relative humidity at 850 hPa reduces significantly in the areas which are cooled at levels below this as a result of passing SKT information to the ocean DA system (cf, Figure 21(b) with Figure 18(a)). This suggests that ocean information is being propagated up through the atmosphere. It is noted that the change in the mean relative humidity does not lead to a significant change in the RMSE in this region (Figure 21(c and d)).

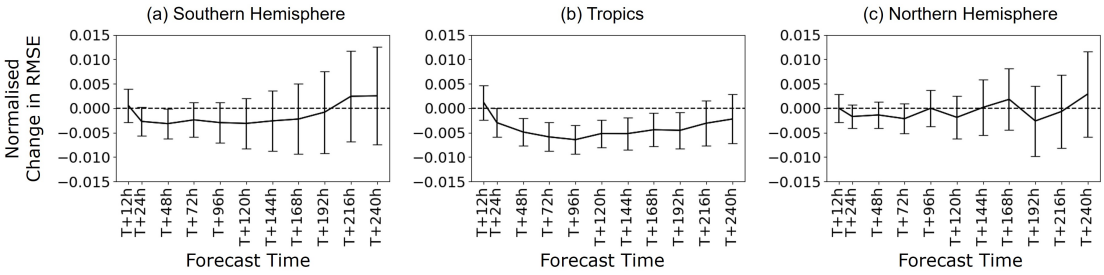

Figure 20: Normalised change in the RMSE of relative humidity at 1000 hPa. Statistics for the regions indicated for the period 2022-06-07 to 2022-08-31 and 2022-12-07 to 2023-02-14.

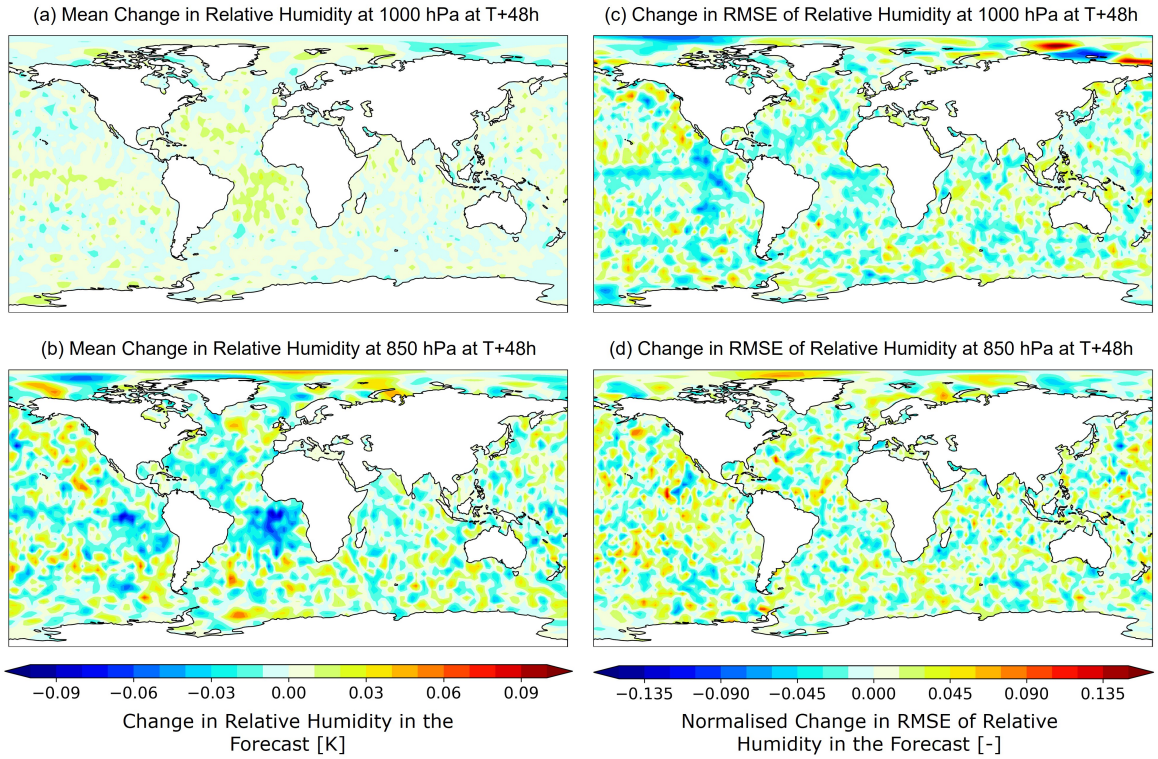

Figure 21: Change in (a) the mean relative humidity forecast field and (b) the normalised RMSE at T+72 hours for 1000 hPa. Global statistics for the period 2022-06-07 to 2022-08-31 and 2022-12-07 to 2023-02-14 for the 00 UTC and 12 UTC cycles.

Another example of the ocean information propagating up through the atmosphere is the change in RMSE for other variables seen at 100 and 200 hPa. Figure 22 shows the normalised change in RMSE of the temperature, vector winds and geopotential height for the first 5 days of the forecast over the Southern Hemisphere. It can be seen that there are statistically significant changes in all variables at T+48h (temperature at 200 hPa in panel d), T+72h (temperature at 100 hPa in panel a, vector winds at 100 and 200 hPa in panels b and e and geopotential height at 200 hPa in panel f) and T+96h (geopotential height at 100 and 200 hPa in panels c and f). These plots are supported by the statistically significant changes in RMSE shown for temperature at T+72h in Figure 18(b) between 30 °S and -60 °S. Similar patterns are seen in both vector winds and geopotential height (not shown).

In addition to the changes in the forecast fields already discussed, there is potential for the use of the SKT estimates from MW imagers to impact the forecast of Tropical Cyclones (TCs). It has previously been shown that, within a coupled system, knowledge of the vertical structure of the ocean is crucial for predicting the development of TCs (Mogensen *et al.*, 2017). The impact of using the SKT estimates from MW imagers in NEMOVAR on the TC forecast has been assessed using the methodology outlined in Magnusson *et al.* (2021). Overall, the impact was neutral (results not shown) and this is likely due to only a few TCs occurring within the study period, making it difficult to obtain statistically meaningful results from the TC verification method.

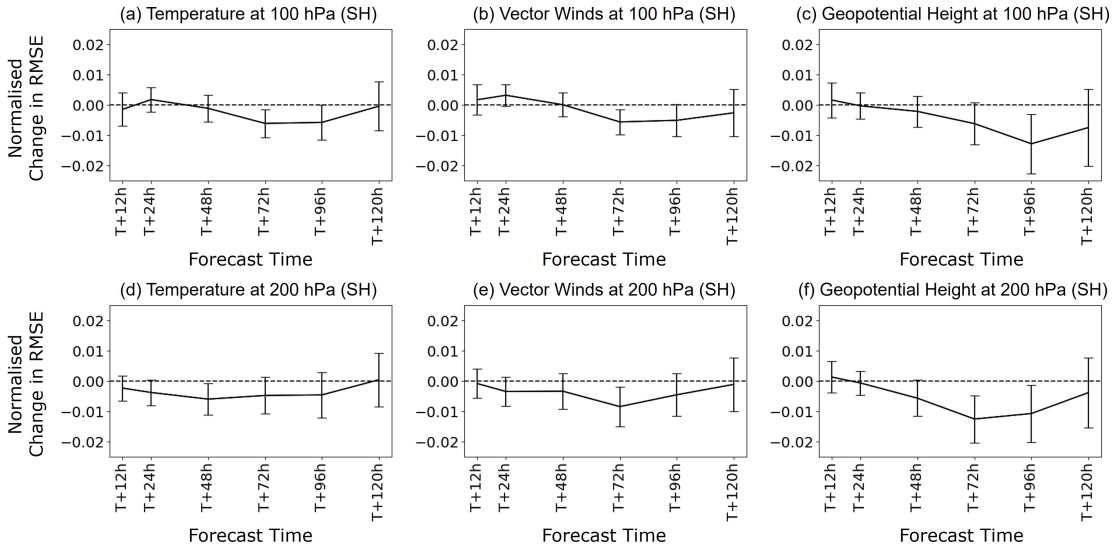

Figure 22: Normalised change in the RMSE of temperature, vector winds and geopotential height at 100 and 200 hPa. Statistics for the regions indicated for the period 2022-06-07 to 2022-08-31 and 2022-12-07 to 2023-02-14.

6 Conclusions

In the current work, information about the ocean skin temperature retrieved in the atmospheric DA system from MW radiances has been passed to the ocean DA system through outer loop and approximate observation operator coupling. This is the first time that information derived from MW radiances have been used in an atmosphere-ocean coupled system to inform the ocean DA system. This represents a major step forward in the exploitation of MW radiances in the IFS as it allows the sensitivity of the observations to both the atmosphere and ocean to be utilised, rather than just the atmosphere.

In this work, the ocean skin temperature information has been derived from two MW imagers: AMSR2 and GMI. Previous work has already demonstrated that retrieved ocean information from these sensors works to correct known deficiencies in the background ocean temperature in an atmosphere only DA system.

Passing these SKT estimates to the ocean DA system has had a positive impact on the fit of ocean observations through decreasing the standard deviation of the background departures for in-situ profiles from ARGO floats. In the Northern Hemisphere, this improvement is statistically significant down to around 25 m depth with the exception of the top-most bin where there are fewer observations available. In the Southern Hemisphere this statistically significant improvement extends to around 75 m depth. These hemispheric improvements reach approximately 0.5% at some levels. But in the Eastern Tropical Pacific, where tropical instability waves lead to fast-changing surface conditions, and where the improved timeliness of the SST information thus appears to be of particular benefit, improvements are seen up to 4% near the surface and these improvements extend down to around 50 m depth.

Validating the model forecasts in terms of the fit to other observations, we see particular improvements in the Significant Wave Height and the geostationary window channels, which have sensitivity to the surface skin temperature.

The largest changes in the forecast fields are in the SST (noting that forecasts beyond 12 hours for subsurface layers are not assessed in this study) and the 2 m temperature (showing somewhat similar patterns to the SST). In terms of the forecast scores for the free atmosphere, the largest impact is in relative humidity in the tropics where the RMSE shows statistically significant improvements from day 2 to day 8. Statistically significant changes are also seen in both the temperature and vector winds are also seen in the southern oceans at day 5. These improvements in the medium range of the forecast indicate that it is taking several days for the changes in the ocean to impact the forecast which is due to the longer timescale on which the ocean operates compared to the atmosphere.

Overall, this work has demonstrated the positive impact on both the ocean and the atmosphere of using outer loop and approximate observation operator coupling to update the ocean near-surface temperature using information derived from MW imagers. In addition, as the maturity of the method develops and other observations with sensitivity the surface are exploited (for example, infra-red or additional MW observations), eventually it will allow the coupled system to be fully constrained by observations, rather than relying on external ocean products.

The method presented here will become operational at the next cycle upgrade of the IFS (to cycle CY50r1). This major step forward in the exploitation of MW radiances is not only important for the currently available MW imagers (i.e. AMSR2 and GMI) but also for upcoming missions such as AMSR3, the Copernicus Imaging Microwave Radiometer (CIMR) from the European Space Agency (ESA) and the Microwave Imager / Ice Cloud Imager (MWI/ICI) from the European Organisation for the Exploitation of Meteorological Satellites (EUMETSAT).

Acknowledgments

Tracy is supported by the EUMETSAT Fellowship Programme.

References

Anderson, E. and Järvinen, H. (1999). Variational quality control. *Quarterly Journal of the Royal Meteorological Society*, **125**(554), 697–722, doi:https://doi.org/10.1002/qj.49712555416, URL https://rmets.onlinelibrary.wiley.com/doi/abs/10.1002/qj.49712555416.

ARGO (2025). ARGO float data and metadata from Global Data Assembly Centre (ARGO GDAC). doi:10.17882/42182, URL 10.17882/42182.

Bauer, P., Geer, A. J., Lopez, P. and Salmond, D. (2010). Direct 4D-Var assimilation of all-sky radiances. Part I: Implementation. *Quarterly Journal of the Royal Meteorological Society*, **136**(652), 1868–1885, doi:doi.org/10.1002/qj.659, URL https://rmets.onlinelibrary.wiley.com/doi/abs/10.1002/qj.659.

Browne, P., de Rosnay, P., Quesada-Ruiz, S., Scanlon, T. and Villeneuve, E. (2025). Coupled observation operators in outer loop coupling data assimilation. *In preparation*.

Browne, P. A., de Rosnay, P., Zuo, H., Bennett, A. and Dawson, A. (2019). Weakly coupled ocean–atmosphere data assimilation in the ECMWF NWP system. *Remote Sensing*, **11**(3), doi:10.3390/rs11030234, URL https://www.mdpi.com/2072-4292/11/3/234.

Chrust, M., Weaver, A. T., Browne, P., Zuo, H. and Balmaseda, M. A. (2025). Impact of ensemble-based hybrid background-error covariances in ECMWF's next-generation ocean reanalysis system. *Quarterly Journal of the Royal Meteorological Society*, **151**(767), e4914, doi:https://doi.org/10.1002/qj.4914, URL https://rmets.onlinelibrary.wiley.com/doi/abs/10.1002/qj.4914.

de Rosnay, P., Browne, P., de Boisséson, E., Fairbairn, D., Hirahara, Y., Ochi, K., Schepers, D., Weston, P., Zuo, H., Alonso-Balmaseda, M., Balsamo, G., Bonavita, M., Borman, N., Brown, A., Chrust, M., Dahoui, M., Chiara, G., English, S., Geer, A., ... and Rabier, F. (2022). Coupled data assimilation at ECMWF: current status, challenges and future developments. *Quarterly Journal of the Royal Meteorological Society*, **148**(747), 2672–2702, doi:10.1002/qj.4330, URL https://rmets.onlinelibrary.wiley.com/doi/abs/10.1002/qj.4330.

Donlon, C., Robinson, I., Casey, K. S., Vazquez-Cuervo, J., Armstrong, E., Arino, O., Gentemann, C., May, D., LeBorgne, P., Piollé, J., Barton, I., Beggs, H., Poulter, D. J. S., Merchant, C. J., Bingham, A., Heinz, S., Harris, A., Wick, G., Emery, B., Minnett, P., Evans, R., Llewellyn-Jones, D., Mutlow, C., Reynolds, R. W., Kawamura, H. and Rayner, N. (2007). The global ocean data assimilation experiment high-resolution sea surface temperature pilot project. *Bulletin of the American Meteorological Society*, **88**(8), 1197 – 1214, doi:10.1175/BAMS-88-8-1197, URL https://journals.ametsoc.org/view/journals/bams/88/8/bams-88-8-1197.xml.

Donlon, C. J., Martin, M., Stark, J., Roberts-Jones, J., Fiedler, E. and Wimmer, W. (2012). The Operational Sea Surface Temperature and Sea Ice Analysis (OSTIA) system. *Remote Sensing of Environment*, **116**, 140–158, doi:10.1016/j.rse.2010.10.017, URL https://www.sciencedirect.com/science/article/pii/S0034425711002197, advanced Along Track Scanning Radiometer (AATSR) Special Issue.

Draper, D. and Newell, D. (2018). Global precipitation measurement (gpm) microwave imager (gmi) after four years on-orbit. In *2018 IEEE 15th Specialist Meeting on Microwave Radiometry and Remote Sensing of the Environment (MicroRad)*, pp. 1–4, doi:10.1109/MICRORAD.2018.8430702.

ECMWF (2021). IFS documentation CY47R3 - part II: Data assimilation. *Technical Report 2*, doi:10.21957/t445u8kna, URL https://www.ecmwf.int/node/20196.

ECMWF (2023). *IFS Documentation CY48R1 - Part IV: Physical Processes*. 4, ECMWF, doi:10.21957/02054f0fbf.

ECMWF (2024). Forecast upgrade improves wind and temperature predictions. URL https://www.ecmwf.int/en/about/media-centre/news/2024/forecast-upgrade-improves-wind-and-temperature-predictions.

Embury, O., Merchant, C. J., Good, S. A., Rayner, N. A., Hoyer, J. L., Atkinson, C., Block, T., Alerskans, E., Pearson, K. J., Worsfold, M., Carroll, N. M. and Donlon, C. (2024). Satellite-based time-series of sea-surface temperature since 1980 for climate applications. *Scientific Data*, **11**(1), 2052–4463, doi:https://doi.org/10.1038/s41597-024-03147-w.

Geer, A. J. (2016). Significance of changes in medium-range forecast scores. *Tellus A: Dynamic Meteorology and Oceanography*, **68**(1), 30229, doi:10.3402/tellusa.v68.30229, URL https://doi.org/10.3402/tellusa.v68.30229.

Geer, A. J. (2024). Joint estimation of sea ice and atmospheric state from microwave imagers in operational weather forecasting. *Quart. J. Roy. Meterol. Soc.*, **150**(763), 3796—3826, URL https://doi.org/10.1002/qj.4797.

Geer, A. J. and Bauer, P. (2010). Enhanced use of all-sky microwave observations sensitive to water vapour, cloud and precipitation. *Technical Report 620*, doi:10.21957/mi79jebka, URL https://www.ecmwf.int/node/9518, also published as EUMETSAT/ECMWF RR20.

Geer, A. J. and Bauer, P. (2011). Observation errors in all-sky data assimilation. *Quarterly Journal of the Royal Meteorological Society*, **137**(661), 2024–2037, doi:10.1002/qj.830, URL https://rmets.onlinelibrary.wiley.com/doi/abs/10.1002/qj.830.

Geer, A. J., Bauer, P. and Lopez, P. (2010). Direct 4D-Var assimilation of all-sky radiances. Part II: Assessment. *Quarterly Journal of the Royal Meteorological Society*, **136**(652), 1886–1905, doi:10.1002/qj.681, URL https://rmets.onlinelibrary.wiley.com/doi/abs/10.1002/qj.681.

Geer, A. J., Lonitz, K., Duncan, D. and Bormann, N. (2022). Improved surface treatment for all-sky microwave observations. *Technical Report 894*, doi:10.21957/zi7q6hau, URL https://www.ecmwf.int/node/20337.

Gentemann, C. L. and Minnett, P. J. (2008). Radiometric measurements of ocean surface thermal variability. *Journal of Geophysical Research: Oceans*, **113**(C8), doi:https://doi.org/10.1029/2007JC004540, URL https://agupubs.onlinelibrary.wiley.com/doi/abs/10.1029/2007JC004540.

Good, S. (2008). NEMOQC. *Available within the ECMWF IFS code base.*

Good, S., Fiedler, E., Mao, C., Martin, M. J., Maycock, A., Reid, R., Roberts-Jones, J., Searle, T., Waters, J., While, J. and Worsfold, M. (2020). The current configuration of the OSTIA system for operational production of foundation sea surface temperature and ice concentration analyses. *Remote Sensing*, **12**(4), doi:10.3390/rs12040720, URL https://www.mdpi.com/2072-4292/12/4/720.

Haiden, T., Dahoui, M., Ingleby, B., de Rosnay, P., Prates, C., Kuscu, E., Hewson, T., Isaksen, L., Richardson, D., Zuo, H. and Jones, L. (2018). Use of in situ surface observations at ECMWF. doi:10.21957/dj9lpy4wa, URL https://www.ecmwf.int/node/18748.

Ingleby, B. and Huddleston, M. (2007). Quality control of ocean temperature and salinity profiles — historical and real-time data. *Journal of Marine Systems*, **65**(1), 158–175, doi:https://doi.org/10.1016/j.jmarsys.2005.11.019, URL https://www.sciencedirect.com/science/article/pii/S0924796306002909, marine Environmental Monitoring and Prediction.

Johnson, G. C. and Fassbender, A. J. (2023). After two decades, ARGO at PMEL, looks to the future. *Oceanography*, **36**, 54–59, URL 10.5670/oceanog.2023.223.

Johnson, G. C., Hosoda, S., Jayne, S. R., Oke, P. R., Riser, S. C., Roemmich, D., Suga, T., Thierry, V., Wijffels, S. E. and Xu, J. (2022). ARGO—two decades: Global oceanography, revolutionized. *Annual Review of Marine Science*, **14**(Volume 14, 2022), 379–403, doi:10.1146/annurev-marine-022521-102008, URL https://www.annualreviews.org/content/journals/10.1146/annurev-marine-022521-102008.

Kazumori, M., Geer, A. and English, S. (2014). Effects of all-sky assimilation of GCOM-W1/AMSR2 radiances in the ECMWF system. *Technical Report 732*, doi:10.21957/dnrgsorja, URL https://www.ecmwf.int/node/10425.

Kazumori, M., Geer, A. J. and English, S. J. (2016). Effects of all-sky assimilation of GCOM-W/AMSR2 radiances in the ECMWF Numerical Weather Prediction system. *Quarterly Journal of the Royal Meteorological Society*, **142**(695), 721–737, doi:https://doi.org/10.1002/qj.2669, URL https://rmets.onlinelibrary.wiley.com/doi/abs/10.1002/qj.2669.

Kilic, L., Prigent, C., Jimenez, C. and Donlon, C. (2021). Technical note: A sensitivity analysis from 1 to 40 GHz for observing the Arctic Ocean with the Copernicus Imaging Microwave Radiometer. *Ocean Science*, **17**(2), 455–461, doi:10.5194/os-17-455-2021, URL https://os.copernicus.org/articles/17/455/2021/.

Lean, P., Geer, A. J. and Lonitz, K. (2017). Assimilation of Global Precipitation Mission (GPM) microwave imager (GMI) in all-sky conditions. *Technical Report 799*, ECMWF, doi:10.21957/8orc7sn33, URL https://www.ecmwf.int/node/17174.

Magnusson, L., Majumdar, S., Emerton, R., Richardson, D., Alonso-Balmaseda, M., Baugh, C., Bechtold, P., Bidlot, J.-R., Bonanni, A., Bonavita, M., Bormann, N., Brown, A., Browne, P., Carr, H., Dahoui, M., Chiara, G. D., Diamantakis, M., Duncan, D., English, S., ... and Rennie, M. (2021). Tropical cyclone activities at ECMWF. doi:10.21957/zzxzzygwv, URL https://www.ecmwf.int/node/20228.

Massart, S., Bormann, N., Bonavita, M. and Lupu, C. (2021). Multi-sensor analyses of the skin temperature for the assimilation of satellite radiances in the European Centre for Medium-Range Weather Forecasts (ECMWF) Integrated Forecasting System (IFS, cycle 47R1). *Geoscientific Model Development*, **14**(9), 5467–5485, doi:10.5194/gmd-14-5467-2021, URL https://gmd.copernicus.org/articles/14/5467/2021/.

McNally, T., Browne, P., Chrust, M., Fairbairn, D., Massart, S., Mogensen, K. and Zuo, H. (2022). Progress on developing a new coupled sea-surface temperature analysis. URL https://www.ecmwf.int/en/newsletter/172/earth-system-science/progress-developing-new-coupled-sea-surface-temperature.

Mogensen, K. and Balmaseda, W. (2012). The NEMOVAR ocean data assimilation system as implemented in the ECMWF ocean analysis for system 4. doi:10.21957/x5y9yrtm, URL https://www.ecmwf.int/node/11174.

Mogensen, K. S., Magnusson, L. and Bidlot, J.-R. (2017). Tropical cyclone sensitivity to ocean coupling in the ECMWF coupled model. *Journal of Geophysical Research: Oceans*, **122**(5), 4392–4412, doi:10.1002/2017JC012753, URL https://agupubs.onlinelibrary.wiley.com/doi/abs/10.1002/2017JC012753.

Morris, T., Scanderbeg, M., West-Mack, D., Gourcuff, C., Poffa, N., Bhaskar, T. V. S. U., Hanstein, C., Diggs, S., Talley, L., Turpin, V., Liu, Z. and Owens, B. (2024). Best practices for core ARGO floats - Part 1: getting started and data considerations. *Frontiers in Marine Science*, **11**, doi:10.3389/fmars.2024.1358042, URL https://www.frontiersin.org/journals/marine-science/articles/10.3389/fmars.2024.1358042.

NERC (2025). NVS Search — vocab.nerc.ac.uk. https://vocab.nerc.ac.uk/search_nvs/RR2/, [Accessed 05-02-2025].

Okuyama, A. and Imaoka, K. (2015). Intercalibration of advanced microwave scanning radiometer-2 (amsr2) brightness temperature. *IEEE Transactions on Geoscience and Remote Sensing*, **53**(8), 4568–4577, doi:10.1109/TGRS.2015.2402204.

Pirro, A., Martellucci, R., Gallo, A., Kubin, E., Mauri, E., Juza, M., Notarstefano, G., Pacciaroni, M., Bussani, A. and Menna, M. (2024). Subsurface warming derived from ARGO floats during the 2022 mediterranean marine heat wave. *State of the Planet*, **4-osr8**, 18, doi:10.5194/sp-4-osr8-18-2024, URL https://sp.copernicus.org/articles/4-osr8/18/2024/.

Roemmich, D., Alford, M. H., Claustre, H., Johnson, K., King, B., Moum, J., Oke, P., Owens, W. B., Pouliquen, S., Purkey, S., Scanderbeg, M., Suga, T., Wijffels, S., Zilberman, N., Bakker, D., Baringer, M., Belbeoch, M., Bittig, H. C., Boss, E., ... and Yasuda, I. (2019). On the future of ARGO: A global, full-depth, multi-disciplinary array. *Frontiers in Marine Science*, **6**, doi:10.3389/fmars.2019.00439, URL https://www.frontiersin.org/journals/marine-science/articles/10.3389/fmars.2019.00439.

Roemmich, D. and Gilson, J. (2009). The 2004–2008 mean and annual cycle of temperature, salinity, and steric height in the global ocean from the ARGO program. *Progress in Oceanography*, **82**(2), 81–100, doi:10.1016/j.pocean.2009.03.004, URL https://www.sciencedirect.com/science/article/pii/S0079661109000160.

Saunders, R., Hocking, J., Turner, E., Havemann, S., Geer, A., Lupu, C., Vidot, J., Chambon, P., Kopken-Watts, C., Scheck, L., Stiller, O., Stumpf, C. and Borbas, E. (2020). RTTOV-13: Science and validation report. URL https://www.ecmwf.int/node/8930.

Scanlon, T., Geer, A., Bormann, N. and Browne, P. (2024). Improving ocean surface temperature for NWP using all-sky microwave imager observations. *Technical Report RR64*, doi:10.21957/c16be07b23.

Shibata, A. (2013). Descriptions of GCOM-W1 AMSR2 level 1r and level 2 algorithms—chapter 4: Sea surface temperature algorithm (NDX-120015a).

Sugiura, N. and Hosoda, S. (2020). Machine learning technique using the signature method for automated quality control of ARGO profiles. *Earth and Space Science*, **7**(9), doi:10.1029/

2019EA001019, URL https://agupubs.onlinelibrary.wiley.com/doi/abs/10.1029/2019EA001019.

Sui, L. and Jiang, Y. (2024). ARGO data anomaly detection based on transformer and fourier transform. *Journal of Sea Research*, **198**, 102483, doi:10.1016/j.seares.2024.102483, URL https://www.sciencedirect.com/science/article/pii/S1385110124000169.

Tan, Z., Cheng, L., Gouretski, V., Zhang, B., Wang, Y., Li, F., Liu, Z. and Zhu, J. (2023). A new automatic quality control system for ocean profile observations and impact on ocean warming estimate. *Deep Sea Research Part I: Oceanographic Research Papers*, **194**, 103961, doi:10.1016/j.dsr.2022.103961, URL https://www.sciencedirect.com/science/article/pii/S0967063722002746.

Wentz, F. J., Gentemann, C., Smith, D. and Chelton, D. (2000). Satellite measurements of Sea Surface Temperature through clouds. *Science*, **288**(5467), 847–850, doi:10.1126/science.288.5467.847, URL https://www.science.org/doi/abs/10.1126/science.288.5467.847.

Wong, A., Keeley, R. and Carval, T. (2024). ARGO quality control manual for CTD and trajectory data. *Technical report*, doi:10.13155/33951.

Wong, A. P. S., Wijffels, S. E., Riser, S. C., Pouliquen, S., Hosoda, S., Roemmich, D., Gilson, J., Johnson, G. C., Martini, K., Murphy, D. J., Scanderbeg, M., Bhaskar, T. V. S. U., Buck, J. J. H., Merceur, F., Carval, T., Maze, G., Cabanes, C., André, X., Poffa, N., ... and Park, H.-M. (2020). ARGO data 1999–2019: Two million temperature-salinity profiles and subsurface velocity observations from a global array of profiling floats. *Frontiers in Marine Science*, **7**, doi:10.3389/fmars.2020.00700, URL https://www.frontiersin.org/journals/marine-science/articles/10.3389/fmars.2020.00700.

Zilberman, N. v., Thierry, V., King, B., Alford, M., André, X., Balem, K., Briggs, N., Chen, Z., Cabanes, C., Coppola, L., Dall'olmo, G., Desbruyères, D., Fernandez, D., Foppert, A., Gardner, W., Gasparin, F., Hally, B., Hosoda, S., Johnson, G. C., ..., Wallace, L. and Van Wijk, E. M. (2023). Observing the full ocean volume using deep ARGO floats. *Frontiers In Marine Science*, **10**, 1287867 (12p.), doi:10.3389/fmars.2023.1287867.

Zuo, H., Alonso-Balmaseda, M., de Boisseson, E., Browne, P., Chrust, M., Keeley, S., Mogensen, K., Pelletier, C., de Rosnay, P. and Takakura, T. (2024). ECMWF's next ensemble reanalysis system for ocean and sea ice: ORAS6. doi:10.21957/hzd5y821lk, URL https://www.ecmwf.int/en/elibrary/81576-ecmwfs-next-ensemble-reanalysis-system-ocean-and-sea-ice-oras6.

Zuo, H., Balmaseda, M. A., Tietsche, S., Mogensen, K. and Mayer, M. (2019). The ECMWF operational ensemble reanalysis–analysis system for ocean and sea ice: a description of the system and assessment. *Ocean Science*, **15**(3), 779–808, doi:10.5194/os-15-779-2019, URL https://os.copernicus.org/articles/15/779/2019/.